A&A 677, A22 (2023)
https://doi.org/10.1051/0004-6361/202346556

Astronomy & Astrophysics

The γ-process nucleosynthesis in core-collapse supernovae

I. A novel analysis of γ-process yields in massive stars

L. Roberti[1,2,3,⋆], M. Pignatari[1,2,4,⋆], A. Psaltis[5,6,⋆], A. Sieverding[7], P. Mohr[8], Zs. Fülöp[8], and M. Lugaro[1,2,9,10]

[1] Konkoly Observatory, Research Centre for Astronomy and Earth Sciences, Eötvös Loránd Research Network (ELKH), Konkoly-Thege Miklós út 15-17, 1121 Budapest, Hungary
[2] CSFK, MTA Centre of Excellence, Budapest, Konkoly-Thege Miklós út 15-17, 1121, Budapest, Hungary
e-mail: lorenzo.roberti@csfk.org
[3] INAF – Osservatorio Astronomico di Roma, Via Frascati 33, 00040 Monteporzio Catone, Italy
[4] E. A. Milne Centre for Astrophysics, University of Hull, Hull HU6 7RX, UK
[5] Department of Physics, North Carolina State University, Raleigh, NC 27695, USA
[6] Triangle Universities Nuclear Laboratory, Duke University, Durham, NC 27710, USA
[7] Max-Planck Institute for Astrophysics, Postfach 1317, 85741 Garching, Germany
[8] Institute for Nuclear Research (ATOMKI), 4001 Debrecen, Hungary
[9] Eötvös Loránd University, Institute of Physics, Budapest 1117, Pázmány Péter sérány 1/A, Hungary
[10] School of Physics and Astronomy, Monash University, VIC 3800, Australia

Received 31 March 2023 / Accepted 15 June 2023

ABSTRACT

Context. The γ-process nucleosynthesis in core-collapse supernovae is generally accepted as a feasible process for the synthesis of neutron-deficient isotopes beyond iron. However, crucial discrepancies between theory and observations still exist: the average yields of γ-process nucleosynthesis from massive stars are still insufficient to reproduce the solar distribution in galactic chemical evolution calculations, and the yields of the Mo and Ru isotopes are a factor of ten lower than the yields of the other γ-process nuclei.
Aims. We investigate the γ-process in five sets of core-collapse supernova models published in the literature with initial masses of 15, 20, and 25 $M_{\odot}$ at solar metallicity.
Methods. We compared the γ-process overproduction factors from the different models. To highlight the possible effect of nuclear physics input, we also considered 23 ratios of two isotopes close to each other in mass relative to their solar values. Further, we investigated the contribution of C–O shell mergers in the supernova progenitors as an additional site of the γ-process.
Results. Our analysis shows that a large scatter among the different models exists for both the γ-process integrated yields and the isotopic ratios. We find only ten ratios that agree with their solar values, all the others differ by at least a factor of three from the solar values in all the considered sets of models. The γ-process within C–O shell mergers mostly influences the isotopic ratios that involve intermediate and heavy proton-rich isotopes with $A > 100$.
Conclusions. We conclude that there are large discrepancies both among the different data sets and between the model predictions and the solar abundance distribution. More calculations are needed; particularly updating the nuclear network, because the majority of the models considered in this work do not use the latest reaction rates for the γ-process nucleosynthesis. Moreover, the role of C–O shell mergers requires further investigation.

Key words. stars: massive – supernovae: general – nuclear reactions, nucleosynthesis, abundances – Sun: abundances

1. Introduction

Neutron–capture processes (see e.g. Käppeler et al. 2011; Cowan et al. 2021 and references therein) made the majority of the nuclei beyond iron in the Solar System. However, these processes are not able to make a number of rare, neutron-deficient, stable isotopes, which constitute a small fraction in mass of the heavy nuclear species. Already in the pioneering work of Burbidge et al. (1957), 35 stable proton-rich nuclides[1] (the p-nuclei) heavier than Fe were identified and the p-process was postulated to explain their existence (see also Cameron 1957). Subsequently, Arnould (1976) demonstrated that p-nuclei can be synthesised through a sequence of (γ,n), (γ,p) and (γ,α) reactions on pre-existing heavy seed material during the latest stages of the hydrostatic evolution of massive stars. Woosley & Howard (1978) showed that the p-process material produced during the pre-supernova evolution is completely reprocessed by the passage of the explosive shock wave; and that the O/Ne-rich layers during core-collapse supernovae (CCSNe) explosions provide the necessary conditions to remake the p-nuclei via a chain of photodisintegrations. These authors called this the γ-process. Prantzos et al. (1990) and then Rayet et al. (1995) performed the first complete computations of the γ-process and provided the sets of yields that were then taken as a reference for studies of the p-nuclei in the following decades (e.g. Arnould & Goriely 2003; Rauscher et al. 2013; Pignatari et al. 2016a and references therein).

⋆ NuGrid Collaboration, http://nugridstars.org
[1] Namely: ^{74}Se, ^{78}Kr, ^{84}Sr, ^{92,94}Mo, ^{96,98}Ru, ^{102}Pd, ^{106,108}Cd, ^{112,114,115}Sn, ^{113}In, ^{120}Te, ^{124,126}Xe, ^{130,132}Ba, ^{136,138}Ce, ^{138}La, ^{144}Sm, ^{152}Gd, ^{156,158}Dy, ^{162,164}Er, ^{168}Yb, ^{174}Hf, ^{180}Ta, ^{180}W, ^{184}Os, ^{190}Pt, and ^{196}Hg.

Not all the heavy proton-rich isotopes are made exclusively by the γ-process. Branching points, either activated by unstable nuclei or by stable isotopes that become unstable at stellar temperature, allow neutron captures to play a role as well. ^{152}Gd and ^{164}Er are representative of this, because they have a potentially dominant *s*-process contribution from low-mass asymptotic giant branch (AGB) stars because of the branching points at ^{151}Sm (unstable in terrestrial conditions) and ^{163}Dy (stable in terrestrial conditions), respectively (see e.g. Arlandini et al. 1999; Bisterzo et al. 2011, 2015). The production of ^{113}In and ^{115}Sn depends on the β-decay of the unstable isomers of the stable nuclides ^{113}Cd and ^{115}In, respectively. However, in this case, their origin is still unclear, with a possible *r*-process contribution (Dillmann et al. 2008). The very long-lived ^{180}Ta isomer with a half-life of greater than 1.2×10^{15} yr may be efficiently produced both by neutrino-spallation reactions on ^{180}Hf (Cumming & Alburger 1985) and the *s*-process (see e.g. Rauscher et al. 2002; Bisterzo et al. 2011). In the latter case, as for ^{163}Dy, ^{179}Hf becomes unstable at stellar temperatures and activates a branching point on the *s*-process path. Finally, ^{138}La might receive a substantial contribution from the neutrino captures on ^{138}Ba (Goriely & Siess 2001). Moreover, new processes have been identified in recent decades that occur in the deepest interior of CCSNe, which may also participate in the production of the lightest *p*-nuclei between Fe and Pd. These processes range from the neutrino-driven winds from the forming neutron star (see e.g. Fröhlich et al. 2006; Arcones & Montes 2011) to the α-rich freeze-out in CCSN ejecta (see e.g. Woosley & Hoffman 1992; Pignatari et al. 2016a), and the *νr*-process proposed very recently by Xiong et al. (2023). Modern multi-dimensional CCSN simulations (e.g. Harris et al. 2017) and calculations of the explosion in spherical symmetry with the inclusion of neutrino heating (e.g. Curtis et al. 2018; Ghosh et al. 2022) suggest that a significant amount of *p*-nuclei yields could be ejected from the innermost layers of the star, especially in the Mo–Ru region (see e.g. Eichler et al. 2017).

Although the γ-process nucleosynthesis in CCSNe has been explored for many decades (see e.g. the reviews Rauscher et al. 2013; Pignatari et al. 2016b and references therein), a complete understanding of the production of *p*-nuclei in stars is still missing, and several discrepancies arise when comparing theoretical model predictions with Solar System abundances. The first fundamental problem is that the average γ-process yields from massive stars are about three times lower than the abundances seen in the Solar System. Furthermore, ^{92,94}Mo and ^{96,98}Ru are systematically underproduced by one order of magnitude compared to the other γ-process nuclei (Arnould & Goriely 2003; Rauscher et al. 2013; Pignatari et al. 2016a). Several works have shown that nuclear uncertainties are not the reason for this substantial disagreement between theory and observations (see e.g. Rapp et al. 2006; Rauscher et al. 2016; Nishimura et al. 2018).

The external layers of thermonuclear supernovae (SNIa) – which result from a white dwarf (WD) accreting material from a stellar binary companion and reaching the Chandrasekhar mass limit – have also been proposed as a site of γ-process nucleosynthesis (Travaglio et al. 2011, 2014; Battino et al. 2020). The first galactic chemical evolution (GCE) calculations made for *p*-nuclei (Travaglio et al. 2018) confirmed that the SNIa scenario would solve the issues related to the γ-process in CCSNe. However, the SNIa solution strongly depends on the number of SNIa generated from Chandrasekhar-mass progenitors within the single-degenerate scenario (Hillebrandt et al. 2013). According to observations, this number is still affected by large uncertainties and could be much lower than required to solve the missing γ-process production (e.g. Woods & Gilfanov 2013; Battino et al. 2020 and references therein).

Given these significant open questions, investigations into potential solutions to boost the production of *p*-nuclei in massive stars – in particular in the Mo–Ru region – are still required. For example, Pignatari et al. (2013) showed that an increase in the ^{12}C+^{12}C reaction rate by two orders of magnitude, as first suggested by Caughlan & Fowler (1988), may lead to an increased Mo and Ru γ-process production up to the level of the other *p*-nuclei, and to an overall increased γ-process efficiency. Also, during the final stages of the evolution of massive stars, the convective O-burning shell may ingest some C-rich material (Rauscher et al. 2002; Meakin & Arnett 2006; Ritter et al. 2018b; Andrassy et al. 2019). This interaction may lead to the formation of an extended merged convective zone, as well as to asymmetries in the stellar structure of the progenitor that might facilitate the CCSN explosion (e.g. Couch & Ott 2013; Müller et al. 2016). During this 'C–O shell merger' event, the C shell material is brought down to the base of the O shell at typical O burning temperature, triggering efficient γ-process nucleosynthesis (Rauscher et al. 2002; Ritter et al. 2018a). The mixing of the *p*-nuclei throughout the extended, mixed C–O shell prevents them from being fully reprocessed by the CCSN shock wave; their yields may therefore increase by orders of magnitude, as compared to models without the C–O shell merger. However, whether or not this scenario can solve some of the puzzles of the missing production of the *p*-nuclei remains to be investigated. Finally, because of the sensitivity of the γ-process to the seeds produced earlier in the evolution by the *s*-process (Costa et al. 2000), Choplin et al. (2022) proposed that an enhanced production of *s*-process seeds in fast-rotating massive stars ('spinstars') at subsolar metallicity could increase the efficiency of γ-process nucleosynthesis and that this contribution could even dominate the solar *p*-nuclei abundance distribution. However, the number of such spinstars as a function of the metallicity is still uncertain and further investigation is required.

To shed further light on the mystery of the γ-process nucleosynthesis in CCSNe, we began a research program dedicated to implementing the latest nuclear reaction rates into new calculations of CCSNe for a wide grid of explosion energies using the most recent version of the NuGrid nucleosynthesis codes (e.g. Pignatari et al. 2016b; Ritter et al. 2018b; Lawson et al. 2022). In this first paper of the series, we present our first step of the program, corresponding to the analysis of the γ-process yields in a number of sets of CCSN models from the literature. The paper is organised as follows: in Sect. 2 we present the sets of CCSN models; in Sect. 3 we describe our method; in Sect. 4 we outline our results; in Sect. 5 we give a brief overview of the current state of the art of nuclear physics for the γ-process; and in Sect. 6 we discuss our results and present our conclusions.

2. Data sets

We consider yields from five sets of CCSN models (Rauscher et al. 2002; Pignatari et al. 2016b; Ritter et al. 2018b; Sieverding et al. 2018; Lawson et al. 2022) with progenitors of initial masses of 15, 20, and 25 $M_\odot$ and solar metallicity. All of the models are based on one-dimensional (1D) computations using different codes and nuclear networks for the hydrostatic evolution, the explosion, and the nucleosynthesis. In the following, we briefly describe the main features of each set.

2.1. Rauscher+02 (RAU)

The data from Rauscher et al. (2002, hereafter labelled RAU15, RAU20, and RAU25 for the three respective masses) are a well-known and widely used set. They were produced using an adaptive nuclear network including up to a maximum number of approximately 2200 nuclear species. The progenitors of the CCSNe were calculated by an updated version of the *Kepler* code (Weaver et al. 1978), while the supernova explosions were simulated using the piston technique (Woosley & Weaver 1995). The explosion energy of the 15 $M_\odot$ model is 1.2×10^{51} erg, according to the assumption for SN 1987A (e.g. Woosley & Haxton 1988), while in the case of 20 and 25 $M_\odot$ models, it is adjusted to obtain the ejection of 0.1 $M_\odot$ of ^{56}Ni. The initial solar composition is from Anders & Grevesse (1989, AG89). The reaction rates involving the nuclei above Fe are mostly from Rauscher & Thielemann (2000), and from Bao et al. (2000) in the case of the (n, γ) reactions. In case of missing experimental information, Rauscher et al. (2002) used the Hauser-Feshbach rates obtained with the NON-SMOKER code (Rauscher et al. 1997). In the case of the two reactions involving p-nuclei, ^{70}Ge$(\alpha, \gamma)^{74}$Se and ^{144}Sm$(\alpha, \gamma)^{148}$Gd, these latter authors implemented the experimental rates from Fülöp et al. (1996) and Somorjai et al. (1998), respectively. Moreover, the rates that shared the same α-potentials as these latter two reactions were recomputed using the same experimental information. The 20 $M_\odot$ model experiences a C–O shell merger about 1 day before the core collapse, forming a single extended mixed convective zone. As mentioned in Sect. 1, the C–O shell merger triggers an efficient γ-process nucleosynthesis during the pre-supernova evolution of the stars that may dominate over the effect of the explosive nucleosynthesis during the CCSN.

2.2. Pignatari+16 (PGN)

The 15, 20, and 25 $M_\odot$ progenitors presented in Pignatari et al. (2016b, hereafter PGN15, PGN20, PGN25, respectively) were computed using the GENEC stellar evolutionary code (Eggenberger et al. 2008) and following the evolution up to and including the central Si burning phase. The further collapse of the Fe core was not followed and the supernova explosion was simulated using a semi-analytical approach, with a prescription for the mass cut provided by Fryer et al. (2012). The adopted initial solar composition is from Grevesse & Noels (1993, GN93). Pignatari et al. (2016b) computed the nucleosynthesis during the evolution and the explosion with the Multi-zone Post-Processing Network – Parallel code (MPPNP; Pignatari & Herwig 2012; Pignatari et al. 2016b; Ritter et al. 2018b), using a dynamical network with a maximum number of 5234 nuclear species. The nuclear network includes 74 313 reactions and above Fe it uses the experimental rates from the KADoNIS compilation (Dillmann et al. 2006) wherever possible for (n, γ) reactions, and the Basel REACLIB database (Rauscher & Thielemann 2000) revision 20090121 for the missing reactions. These models present some interesting features regarding the γ-process nucleosynthesis. In the PGN15 model, the mass-cut is deep enough to allow the ejection of some α-rich freeze-out material, slightly increasing the yields of the lightest γ-process nuclei. In the PGN20 model, the shock wave accelerates at the interface between CO and the He core because of the steep density gradient. This results in an increase in the peak temperature, which leads to reactivation of the γ-process nucleosynthesis. In the PGN25 model, the γ-process occurs in a narrow region of the star that unfortunately lacks in spatial resolution; this prevents us from distinguishing the abundance peaks of all the p-nuclei. For this reason, we decided to exclude this model from the discussion in the following sections.

2.3. Ritter+18 (RIT)

The set of Ritter et al. (2018b, RIT15, RIT20, RIT25) is the product of follow-up work based on the results of Pignatari et al. (2016b), except that the stellar progenitors were calculated with the `MESA` code (Paxton et al. 2011). The main features of the RIT models are the same as in the PNG models (initial composition, physics inputs, explosion mechanism, and nucleosynthesis code), but some parts of the reaction network database are updated and, as mentioned above, a different code (`MESA`) is used to compute the stellar progenitors. The RIT models adopt the JINA REACLIB reaction rate library V1.1 (Cyburt 2011) instead of the Basel REACLIB database used in the PNG models. The use of a different stellar code led to several significantly different results. The RIT15 model experiences a C–O shell merger event, similarly to the RAU20 model, and the production of the γ-process nuclei greatly increases in the pre-supernova evolution. The RIT20 model has a large amount of fallback material after the explosion –such that only the region above explosive Ne burning is ejected– and ends with a remnant mass of 2.7 $M_\odot$. Moreover, in this star, the convective C–shell is particularly extended and is able to efficiently activate the ^{22}Ne neutron source, triggering the s-process nucleosynthesis. The RIT25 model experiences such significant fallback that the explosion ends in a failed supernova, locking all the explosive nucleosynthesis material into the central remnant of 5.7 $M_\odot$.

2.4. Sieverding+18 (SIE)

The set from Sieverding et al. (2018, SIE15, SIE20, SIE25) is based on stellar progenitors calculated using the *Kepler* code, as in the RAU models, and with the same explosion energy equal to 1.2×10^{51} erg, but with different choices for several physical and numerical parameters. The initial solar composition is from Lodders (2003, L03). The nuclear network used for the stellar evolution calculations is not identical to the reaction network used for the explosion. While the former is mostly identical to the RAU models, the latter includes the JINA REACLIB reaction rate library V2.2, and an updated ν-induced reaction rate set. The rate of the neutron–capture reaction ^{137}La$(n, \gamma)^{138}$La is instead from a previous version of REACLIB presented by Rauscher & Thielemann (2000). The inclusion of ν-induced reactions is crucial for the production of the two p-nuclei ^{138}La and ^{180}Ta, which are directly produced by ν_e capture on the corresponding isobars (Woosley et al. 1990). Sieverding et al. (2018) presented a parametric study of the explosive yields using several neutrino energies. Here we include the same set as in den Hartogh et al. (2022); these are the models with the highest neutrino energy.

2.5. Lawson+22 (LAW)

The stellar progenitors of Andrews et al. (2020) and Lawson et al. (2022, LAW15, LAW20, LAW25) were computed with a recent version of the *Kepler* code (Heger & Woosley 2010), while a 1D hydrodynamic code was used for the explosion, mimicking a 3D convective engine (Fryer et al. 1999, 2018). The hydrostatic nucleosynthesis was calculated via the MPPNP code (as PNG and RIT), while the Tracer particle Post-Processing

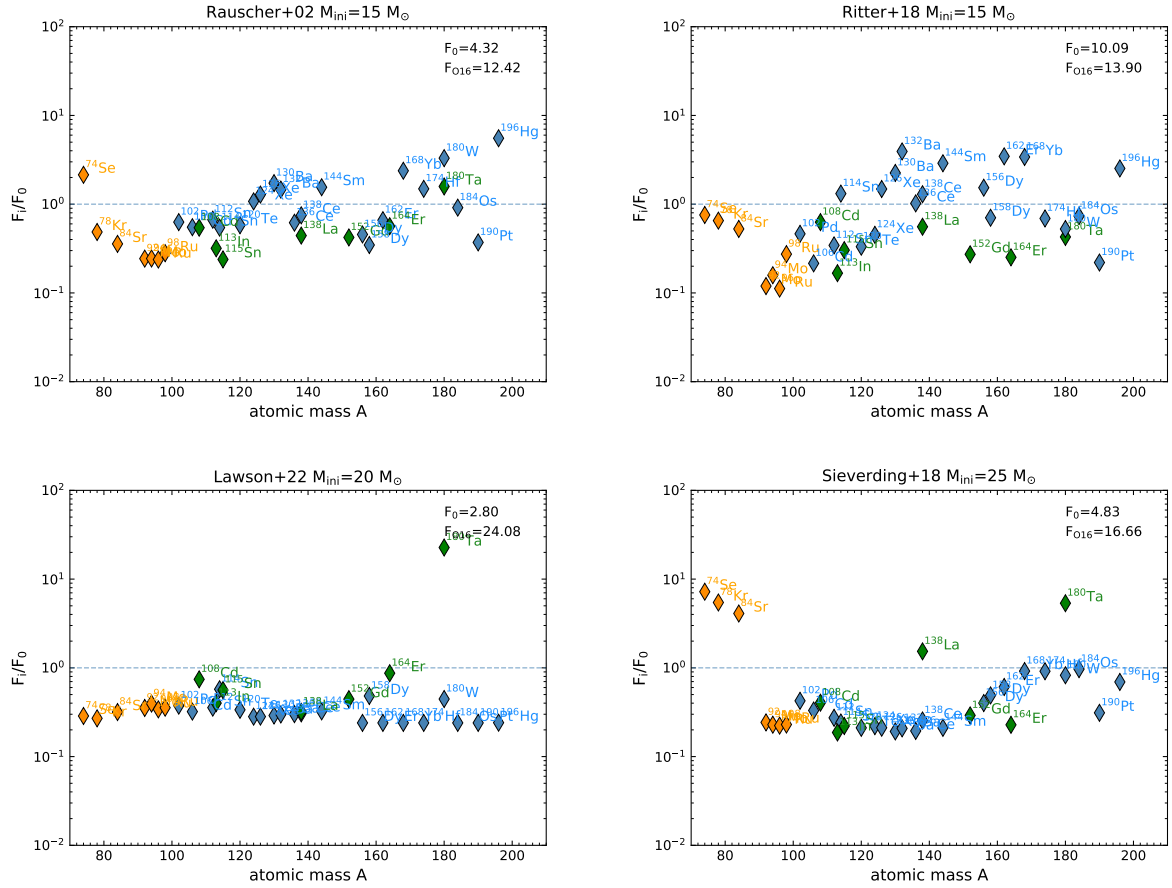

Fig. 1. p-nuclide overproduction factors divided by their average (Eq. (1)), the value of which is indicated in the top right of each panel, together with the OP factor for ^{16}O (F_{O16}) for comparison. The blue, orange, and green symbols respectively represent: (i) nuclei produced exclusively by the γ-process, (ii) nuclei that may have an additional explosive contribution; and (iii) nuclei that also have s-, r-process, or neutrino-capture contributions. Four examples of representative models are shown: the upper left panel is RAU15, a typical model; the upper right panel is RIT15, a case where the C–O shell merger occurs; the lower left panel is LAW20, a failed supernova; and the lower right panel is SIE25, a model where the F_0 is the same as for the typical RAU15 model shown in the upper left panel, but where this value is driven by two isotopes produced by neutrino captures rather than by the p-nuclei produced exclusively by the γ-process (Sieverding et al. 2018). We note that in the two bottom panels a large number of p-nuclei – including the Mo and Ru isotopes – share the same $F_i/F_0 \simeq 0.2$–0.3. However, as shown by the low F_0, there is no significant production of these isotopes and their pattern only reflects the initial solar abundance distribution used in the models.

Network – Parallel code (TPPNP; Jones et al. 2019) was used for the explosive nucleosynthesis. The initial solar composition is GN93, as in the RIT models. The stellar yields for the whole stellar set including the models used in this work are available online (Andrews et al. 2020). As in RIT20, in the LAW25 model the C–shell is also particularly extended and has an efficiently active neutron source. Again, similarly to RIT20, LAW20 shows significant fallback and all the explosive nucleosynthesis is confined within an innermost smaller mass of 2.2 $M_\odot$ at the position of the final mass cut. Therefore, the ejecta of this model contains only the material ejected from the C shell outwards.

3. Average overproduction factors

The overproduction (OP) factor for each isotope is defined as OP = $X/X_\odot$, which is the ratio between its mass fraction X – which is equal to the total integrated yield divided by the total mass ejected – and the solar mass fraction $X_\odot$, for which we use the values of Asplund et al. (2009)[2]. A useful parameter to evaluate the efficiency of the γ-process nucleosynthesis is F_0, defined as the average of the OP factors of all the 35 p-nuclei, that is:

$$F_0 = \frac{\sum_{i=1}^{35} F_i}{35}, \quad (1)$$

where F_i is the OP factor of the p-nuclide i. The value of F_0 has been taken over the years as the representative feature of γ-process nucleosynthesis and has been used as a normalisation factor for the single p-nuclei OP factors; that is, F_i/F_0 measures the deviation of the production of each single isotope i from the average production. Figure 1 shows the F_i/F_0 distribution for a selection of models. The same figure for each model can be found in Appendix A, together with a figure showing the OP factors of all 35 p-isotopes.

Two fundamental features are highlighted from the figure and from the distributions of all the models. First, there are large variations of both the OP factors and of F_0 with the initial mass of the stellar progenitor. Depending on the set of models considered, F_0 varies by up to a factor of roughly five, with even larger variation for the OP of single isotopes. This scatter is much larger than that found in previous studies (e.g. Rayet et al. 1995), supporting the idea that γ-process nucleosynthesis does

[2] For the p-only isotopes, these values are the same as those given in the other solar abundance compilations used in the different models as described in the previous section.

Table 1. Percentages of p-nuclei yields in C–O mergers.

Isotope	Explosive (%)	Merger (%)	Envelope (%)	Explosive (%)	Merger (%)	Envelope (%)
	RIT15			RAU20		
^{74}Se	**74.1**	14.9	10.9	47.3	49.0	3.6
^{78}Kr	**82.1**	5.9	11.9	**62.1**	28.8	9.1
^{84}Sr	**70.5**	11.5	17.4	42.7	**53.2**	4.0
^{92}Mo	6.4	8.4	**85.2**	10.5	15.0	**74.5**
^{94}Mo	2.8	27.4	**69.7**	5.9	45.6	48.3
^{96}Ru	8.2	4.3	**87.5**	12.1	2.4	**85.5**
^{98}Ru	13.1	49.6	37.2	16.7	37.9	45.3
^{102}Pd	36.4	40.2	23.3	45.1	25.6	29.2
^{106}Cd	34.6	22.5	43.0	**53.5**	9.2	37.3
^{108}Cd	11.4	**63.4**	25.1	19.1	46.2	34.6
^{112}Sn	34.6	35.5	29.8	47.0	16.9	36.1
^{114}Sn	20.7	**71.0**	8.2	18.0	**68.7**	13.0
^{115}Sn	0.3	**64.9**	34.8	1.3	**61.7**	36.8
^{113}In	5.4	42.5	**52.0**	8.5	46.6	44.7
^{120}Te	8.2	**62.5**	29.3	43.0	29.6	27.3
^{124}Xe	22.0	**59.9**	18.1	**70.3**	8.9	20.8
^{126}Xe	7.0	**87.4**	5.5	40.1	**54.1**	5.6
^{130}Ba	35.0	**61.0**	3.7	**66.6**	24.1	9.3
^{132}Ba	1.8	**95.9**	2.2	18.6	**78.9**	2.2
^{136}Ce	40.4	**51.0**	8.5	42.6	39.0	18.4
^{138}Ce	8.3	**84.7**	6.8	20.7	**74.4**	4.6
^{138}La	0.0	**82.9**	17.0	2.0	**91.6**	6.2
^{144}Sm	12.6	**84.0**	3.2	16.3	**80.6**	2.9
^{152}Gd	0.0	3.9	**96.1**	0.5	13.1	**86.1**
^{156}Dy	0.6	**93.7**	5.7	7.7	**89.5**	2.3
^{158}Dy	0.0	**84.4**	15.5	1.8	**95.8**	1.9
^{162}Er	0.3	**97.2**	2.4	3.6	**95.0**	1.0
^{164}Er	7.5	39.1	**53.3**	16.4	**70.7**	12.7
^{168}Yb	2.4	**94.4**	3.2	3.8	**95.1**	0.7
^{174}Hf	3.7	**87.5**	8.6	6.7	**92.2**	1.4
^{180}Ta	0.0	**98.3**	1.7	0.9	**94.7**	4.2
^{180}W	18.1	**70.7**	10.2	35.0	**61.8**	3.1
^{184}Os	0.9	**88.9**	10.2	0.8	**96.8**	2.3
^{190}Pt	1.2	**58.4**	40.3	3.5	**91.4**	4.8
^{196}Hg	12.1	**84.4**	2.7	14.9	**84.2**	0.6

Notes. Percentages of the total p-nuclei yields of the two models with the C–O merger (RIT15 and RAU20) in three parts of the ejecta: the zone dominated by the explosive nucleosynthesis ("explosive"), the zone of the mixed C–O shell ("merger"), and the zone from the He shell outwards ("envelope"). Contributions are highlighted in bold when larger than 50%.

not depend significantly on the progenitor mass. Second, large variations are also present when we compare models with the same progenitor mass but from different sets. This is because the p-nuclei abundances do not depend only on the progenitor mass and the explosion energy. Rather, they are a complex product of the combination of conditions in the stellar progenitor layers and the interaction of those layers with the CCSN shock (e.g. Rauscher et al. 2002; Ritter et al. 2018b).

The F_0 is often compared to the OP factor of the nuclide ^{16}O (hereafter $F_{\rm O16}$), one of the main products of CCSNe. This allows us to approximately quantify the contribution from massive stars to the solar abundances of the p-nuclei without using GCE calculations. If the p-nuclei and ^{16}O share the same production site, one would expect that $F_0 \sim F_{\rm O16}$; however, Rayet et al. (1995) already found an underproduction of at least a factor of 2, that is, $F_0/F_{\rm O16} \simeq 0.5$. Pignatari et al. (2013) confirmed this result and pointed out that the p-nuclei underproduction is probably more severe, because at solar metallicity, twice as many secondary nucleosynthetic products – such as γ-process nuclei – should be synthesised as primary isotopes, such as ^{16}O (see e.g. Tinsley 1980). All the models in our sets have $F_0 \lesssim F_{\rm O16}$, except for PGN15, where $F_0/F_{\rm O16} \sim 1.05$, which is still far from the factor of roughly two required to reproduce the solar abundances.

Relative to a typical model (e.g. top left panel of Fig. 1), models with a C–O shell merger (top right panel) can significantly contribute to the production of γ-process nuclei, which is made evident when comparing the values of F_0 and $F_{\rm O16}$ in these two panels. Nevertheless, in these same models, F_0 does not exceed $F_{\rm O16}$. In both the RIT15 and RAU20 models, the effect of the C–O shell merger is dominant on the yields of most of the p-isotopes with $A \gtrsim 110$ (see Table 1). The production of the lightest isotopes is instead less clear: the RAU20 merger

Table 2. Definition of average overproduction factors.

F	Excluded contribution	Excluded isotopes
F_0	–	–
$F_0^{\rm I}$	*s*-, *r*-process, *ν*-capture, *νp*-process, *α*-rich freeze-out	^{74}Se, ^{78}Kr, ^{84}Sr, ^{92,94}Mo, ^{96,98}Ru, ^{108}Cd, ^{113}In, ^{115}Sn, ^{138}La, ^{152}Gd, ^{164}Er, ^{180}Ta
$F_0^{\rm II}$	*νp*-process, *α*-rich freeze-out	^{74}Se, ^{78}Kr, ^{84}Sr, ^{92,94}Mo, ^{96,98}Ru
$F_0^{\rm III}$	*s*-, *r*-process, *ν*-capture	^{108}Cd, ^{113}In, ^{115}Sn, ^{138}La, ^{152}Gd, ^{164}Er, ^{180}Ta
F_γ	*s*-, *r*-process, *ν*-capture, *νp*-process, *α*-rich freeze-out, partly the *γ*-process	all but the 3 most produced *γ*-only nuclei

component is comparable to the explosive component, while the RIT15 merger component is less relevant. When one element has more than one isotope produced by the *γ*-process, the C–O shell merger favours the synthesis of the more neutron-rich isotopes, such as ^{94}Mo, ^{98}Ru, ^{108}Cd, ^{114}Sn, partially ^{115}Sn, ^{126}Xe, ^{132}Ba, ^{138}Ce, partially ^{158}Dy, but not ^{164}Er; we note that this latter has a dominant contribution from the *s*-process (Appendix B.9). These properties indicate that the *γ*-process in C–O shell mergers operates at lower temperatures (those typical of O burning at the bottom of the convective shell), as compared to the explosion.

As not all the *p*-nuclei have a *γ*-only origin, F_0 might not correctly reflect production from the *γ*-process. For example, in the case of a failed supernova (such as the LAW20 shown in the bottom left panel of Fig. 1, and RIT25), F_0 could be dominated by isotopes with additional nucleosynthetic contributions besides the *γ*-process, such as ^{180}Ta in LAW20. Neutrino processes producing ^{138}La and ^{180}Ta contributed the most to the F_0 value in SIE25 (lower right panel of Fig. 1). Therefore, to better constrain the *γ*-process itself, we decided to define additional averaged values similar to F_0 ($F_0^{\rm I}$, $F_0^{\rm II}$, $F_0^{\rm III}$, and $\rm F_\gamma$) by excluding different isotope groups, as listed and described in Table 2. Among the various excluded isotopes, ^{108}Cd is traditionally considered a *γ*-only isotope; however, in the models considered here we find that ^{108}Cd can also be produced by neutron captures starting on ^{107}Ag. This production may be non-negligible, because the solar abundance of ^{107}Ag used in the models as initial is more than 15 times larger than the solar abundance of ^{108}Cd. For this reason, we included this isotope among the nuclei with an additional contribution. Our new definitions help us to identify why some models do not produce *p*-nuclei but nevertheless have relatively high F_0 values. Table 3 lists all the different *F*-values in our sets of models.

When comparing all these different values to $F_{\rm O16}$, we find no significant improvement using $F_0^{\rm I}$, $F_0^{\rm II}$, or $F_0^{\rm III}$ instead of F_0. Using F_γ, instead, we find six models with values larger than $F_{\rm O16}$, of which four models (RAU20, PGN20, RIT15 and RIT20) have $F_\gamma/F_{\rm O16} > 2$. ^{196}Hg contributes to the F_γ of three out of these four models, and ^{130}Ba and ^{168}Yb to two. Overall, we conclude that *F*-values should be used carefully as by including many OP factors in the average can hide information. Moreover, different CCSN models may efficiently produce different single or groups of *p*-nuclei, and still result in a low value of F_0. Therefore, the use of the *F*-values only is not enough to investigate the properties of the *γ*-process nucleosynthesis and an accurate analysis of the production of the single isotopes is required instead.

4. Isotopic ratios

We analysed the correlations between 12 different couples of OP ratios (for a total of 23 ratios given that one ratio is used twice). We chose ratios of isotopes close in mass in order to study the local properties of the *γ*-process production, which are also affected by the impact of the different sets of reaction rates used in the different sets of models. We avoided including more than one isotope with additional contribution(s) beyond the *γ*-process in each couple of ratios. While the OP factor quantifies the absolute production of a given isotope relative to solar, and therefore indicates whether or not this production is significant, the ratio of two OP factors quantifies the overproduction of the two isotopes relative to each other. Therefore, if an OP ratio agrees with solar, then the two isotopes have similar OP factors; if it does not, then they have different OP factors.

Usually, comparisons with solar abundances are made using yields averaged over the initial mass function (IMF) because the solar composition is the result of Galactic chemical evolution with contributions from many stars. We do not proceed in this way here because, first, a comparison among different single-star yields allows us to study the *γ*-process in different stellar conditions in detail and to check whether or not there exist superior candidates that can reproduce the solar isotopic ratios. Travaglio et al. (2018) already showed that, with the current generation of massive star yields, it is not possible to explain the *γ*-process solar distribution using GCE. New GCE calculations with the yields computed using the updated reaction rates for the *γ*-process will be explored in future work. Second, our analysis also focuses on the C–O shell mergers and at present, the frequency and the relation of such events with initial mass is unknown. Third, most of the sets of models available in the literature do not include a sufficient number of initial masses and/or metallicities, and if they do, the size of the nuclear network is too limited to produce reliable yields for the *γ*-process nucleosynthesis. This makes the use of IMF-averaged yields not particularly meaningful in comparisons with solar composition.

The differences in stellar modelling (e.g. different choices of convection, overshooting, etc.) and in nuclear physics (e.g. number of explicitly included nuclear species, reaction rate database, etc.) introduce a significant source of uncertainty and make it difficult to define the extent to which a result is in agreement with the solar distribution. To account for this, we consider models to be in relatively good agreement with solar when both of the following conditions are satisfied: (i) they fall to within a factor of three from the solar ratio and (ii) they have an overproduction of at least twice solar (OP > 2).

In the following, we summarise the main results of our analysis. An extended discussion for each of the 12 couples of isotopic ratios is presented in Appendix B. As already mentioned in Sect. 2, we do not include the two faint supernova models (LAW20 and the RIT25) because the *γ*-process yields remain locked in the compact remnant and only the envelope of the star is ejected into the interstellar medium. We also excluded the PGN25 model due to a lack of resolution in the *γ*-process abundance peaks. Table 4 collects the main results for each isotopic ratio. We note that the analysis reported below will need to be complemented by future studies where each of the isotopic ratios discussed here is carefully investigated in terms of

Table 3. Average overproduction factors in the models.

Model	F_0	F_{O16}	F_0^I	F_0^{II}	F_0^{III}	F_γ	F_γ isotopes
RAU15	4.32E+00	1.24E+01	5.53E+00	4.78E+00	4.76E+00	**1.61E+01**	^{196}Hg, ^{180}W, ^{168}Yb
RAU20 [(a)]	1.79E+01	2.68E+01	2.54E+01	2.06E+01	2.08E+01	**8.91E+01**	^{168}Yb, ^{196}Hg, ^{162}Er
RAU25	1.56E+01	4.80E+01	1.37E+01	1.31E+01	1.68E+01	3.59E+01	^{196}Hg, ^{180}W, ^{130}Ba
PGN15	**5.03E+00**	4.72E+00	2.93E+00	2.95E+00	**5.54E+00**	**5.64E+00**	^{130}Ba, ^{132}Ba, ^{168}Yb
PGN20	**1.86E+01**	1.85E+01	**2.15E+01**	1.79E+01	**2.14E+01**	**4.93E+01**	^{196}Hg, ^{130}Ba, ^{180}W
RIT15 [(a)]	1.01E+01	1.39E+01	**1.43E+01**	1.17E+01	1.17E+01	**3.63E+01**	^{132}Ba, ^{162}Er, ^{168}Yb
RIT20	1.66E+01	1.94E+01	1.40E+01	1.34E+01	1.78E+01	**4.34E+01**	^{196}Hg, ^{130}Ba, ^{136}Ce
(RIT25)	2.12E+00	1.94E+01	6.81E-01	2.47E+00	6.95E-01	8.70E-01	^{114}Sn, ^{158}Dy, ^{168}Yb
SIE15	2.78E+00	6.09E+00	3.05E+00	3.02E+00	2.75E+00	5.89E+00	^{196}Hg, ^{180}W, ^{130}Ba
SIE20	3.57E+00	1.24E+01	2.53E+00	3.05E+00	3.31E+00	6.01E+00	^{196}Hg, ^{180}W, ^{168}Yb
SIE25	4.83E+00	1.67E+01	2.09E+00	2.99E+00	4.62E+00	4.51E+00	^{184}Os, ^{168}Yb, ^{174}Hf
LAW15	4.13E+00	1.26E+01	4.87E+00	4.72E+00	4.10E+00	9.56E+00	^{190}Pt, ^{196}Hg, ^{158}Dy
(LAW20)	2.80E+00	2.41E+01	8.88E-01	3.27E+00	8.98E-01	1.40E+00	^{102}Pd, ^{158}Dy, ^{180}W
LAW25	1.49E+01	5.18E+01	1.50E+01	1.62E+01	1.36E+01	3.10E+01	^{130}Ba, ^{184}Os, ^{158}Dy

Notes. Values of the quantities defined in Table 2 and the reference ^{16}O overproduction factor F_{O16} for all the models. The last column indicates the three most produced γ-only nuclei on which the calculation of the reported F_γ is based. Values highlighted in bold are larger than F_{O16} for every model. The models in parenthesis are not included in our analysis of the isotopic ratios presented in Sect. 4. [(a)]These two models experience the C–O shell merger.

both the nuclear physics input (see also Sect. 5) and the different modelling approaches.

There are 10 ratios that satisfy both of our conditions for a good agreement with the solar ratio for most of the models (^{74}Se/^{78}Kr, ^{84}Sr/^{78}Kr, ^{102}Pd/^{108}Cd, ^{106}Cd/^{108}Cd, ^{120}Te/^{126}Xe, ^{124}Xe/^{126}Xe, ^{130}Ba/^{132}Ba, ^{136}Ce/^{138}Ce, ^{144}Sm/^{132}Ba, and ^{174}Hf/^{180}W); the other 13 ratios either have low OP factors or are further than a factor of three from solar. We find a general agreement with the solar ratios involving the lightest p-nuclei, except in the case of Mo and Ru isotopes. We note that no model satisfies the condition OP > 2 for ^{92}Mo, ^{94}Mo, ^{96}Ru, and ^{98}Ru. The production of the isotopes between ^{74}Se and ^{108}Cd is mostly dominated by the γ-process happening during the explosion, even in the models with C–O shell mergers.

The majority of the ratios involving heavier isotopes present a significant contribution from radiogenic species. In some cases, the radiogenic contribution can be the determining factor in either reaching good agreement with the solar ratio (e.g. ^{120}Te/^{126}Xe, ^{124}Xe/^{126}Xe) or conversely in moving away from solar (e.g. ^{156}Dy/^{158}Dy, ^{184}Os/^{196}Hg, ^{190}Pt/^{196}Hg).

As mentioned in Sect. 3, the overproduction of p-nuclei with $A \gtrsim 110$ largely increases in models with C–O shell mergers (RIT15 and RAU20). Moreover, these models have generally larger overproduction of the more neutron rich p-nuclei. There are nine isotopic ratios in which the C–O shell mergers stand out from the other models. In four cases (^{144}Sm/^{152}Gd, ^{156}Dy/^{152}Gd, ^{162}Er/^{164}Er, and ^{168}Yb/^{180}Ta), the isotopic ratio from the merger is closer to solar than in the standard models. The opposite occurs in the other four cases (^{112}Sn/^{114}Sn, ^{120}Te/^{126}Xe, ^{124}Xe/^{126}Xe, ^{130}Ba/^{132}Ba, and ^{136}Ce/^{138}Ce).

Of the 23 ratios, 8 include one isotope with an additional nucleosynthetic contribution besides the γ-process (see Sects. 1 and 3, and Table 4). We used the results from the GCE computation of Bisterzo et al. (2014) and from Nemeth et al. (1994), Theis et al. (1998) and Dillmann et al. (2008) to estimate the neutron-capture contribution to the p-nuclei in the solar composition and derive the residual component, which is possibly dominated by the γ-process. There are instead no quantitative predictions for the other explosive components (e.g. α-rich freeze-out, νp-process). The models only show good agreement with the residual solar ratios in four cases: ^{112}Sn/^{114}Sn, ^{113}In/^{114}Sn, ^{115}Sn/^{114}Sn, and ^{144}Sm/^{152}Gd. In the other four cases (^{138}La/^{132}Ba, ^{156}Dy/^{152}Gd, ^{162}Er/^{164}Er and ^{168}Yb/^{180}Ta), the (residual) solar ratio is always underestimated.

5. Nuclear physics considerations

The models included in our analysis (except for RAU) were computed in the last decade and the nuclear physics inputs included in these calculations cover a time span of about 25 yr. The RAU models use mostly an early version of the Basel REACLIB (Rauscher & Thielemann 2000) compilation and the neutron-capture rates from Bao et al. (2000). In the case of missing experimental information, the models include the Hauser-Feshbach rates obtained with the NON-SMOKER code (Rauscher et al. 1997). The PGN models adopt the KADoNIS compilation (Dillmann et al. 2006) for experimental neutron-capture rates and the Basel REACLIB (revision 20090121) compilation is used in all other cases. The RIT models use KADoNIS for experimental neutron-captures and the JINA REACLIB, 20120510 V1.1 (Cyburt 2011) compilation for theoretical neutron-capture rates and charged-particle reaction rates. The LAW models use the KADoNIS compilation for experimental neutron-captures and the most recent version of the JINA REACLIB compilation (V2.2) in all the other cases. The SIE models adopt the same version of JINA REACLIB as LAW models, but only for the explosive nucleosynthesis. The γ-process nucleosynthesis yields presented in this work were therefore computed with outdated reaction rates and new calculations are required to test the impact of the most recent recommendations discussed below.

Experimental data at energies relevant for γ-process nucleosynthesis are rather scarce, and for this reason there is strong interest from the low-energy nuclear physics community to measure reaction cross sections that are related to the synthesis of p-nuclei. Typically, α-induced reaction cross sections are smaller than their p-induced counterparts because of the higher Coulomb barrier, and consequently the measurements are more

Table 4. 23 isotopic ratios.

Isotopic ratio	Subsection	Subsolar	Solar	Super-solar	Merger	Radiogenic	Additional components
^{74}Se/^{78}Kr	B.1	0	7	5			α
^{84}Sr/^{78}Kr	B.1	0	11	1			α
^{92}Mo/^{94}Mo	B.2	0	12	0			α
^{96}Ru/^{98}Ru	B.2	0	12	0			α
^{102}Pd/^{108}Cd	B.3	0	12	0			
^{106}Cd/^{108}Cd	B.3	0	12	0			
^{112}Sn/^{114}Sn	B.4	1	11	0	v		s,r
^{113}In/^{114}Sn	B.4	4	8	0		v	s,r
^{115}Sn/^{114}Sn	B.4	1	11	0	v		s,r
^{120}Te/^{126}Xe	B.5	2	10	0	v	v	
^{124}Xe/^{126}Xe	B.5	2	10	0	v		
^{130}Ba/^{132}Ba	B.6	1	9	1	v	v	
^{136}Ce/^{138}Ce	B.6	1	9	1	v	v	
^{138}La/^{132}Ba	B.7	8	3	1		v	ν
^{144}Sm/^{132}Ba	B.7	0	11	1		v	
^{144}Sm/^{152}Gd	B.8	4	8	0			s
^{156}Dy/^{152}Gd	B.8	6	6	0		v	s
^{156}Dy/^{158}Dy	B.9	2	10	0		v	
^{162}Er/^{164}Er	B.9	7	5	0	v	v	s
^{168}Yb/^{180}Ta	B.10	10	2	0	v	v	s,ν
^{174}Hf/^{180}W	B.10	0	12	0	v	v	
^{184}Os/^{196}Hg	B.11	4	8	0		v	
^{190}Pt/^{196}Hg	B.11	9	3	0		v	

Notes. The 23 isotopic ratios are plotted in Figs. B.1–B.11. The columns 'Subsolar', 'Solar' and 'Super-solar' identify the number of models that fall below, within, and above a factor of 3 from the solar γ-process component, respectively. The column 'Merger' reports 'v' if at least one of the two yields of the isotopic ratio is dominated by the merger (corresponding to the bold highlighted components in Table 1). The column 'Radiogenic' reports 'v' if at least one of the two isotopes of the ratio has a significant radiogenic contribution. The column 'Additional components' lists the possible additional nucleosynthetic processes that may contribute to at least one of the two isotopes of the ratio; possible additional contributions are: α (α-rich freeze-out or different explosive component), s (s-process), r (r-process), ν (neutrino capture).

challenging. As noted in the latest γ-process nucleosynthesis review by Pignatari et al. (2016a), many new measurements have been performed on the (p,γ), (α,γ), and (α,n) reactions that produce or destroy p-nuclei.

In addition to widely used techniques, such as in-beam γ-spectroscopy (see Khaliel et al. 2017; Foteinou et al. 2018; Psaltis et al. 2019; Wu et al. 2020; Heim et al. 2020 for some examples), the activation method (see Korkulu et al. 2018; Gyürky et al. 2019; Scholz et al. 2020; Cheng et al. 2021 and references therein), and the total absorption spectroscopy (TAS)/4π summing method (Kelmar et al. 2020; Harissopulos et al. 2021; Palmisano-Kyle et al. 2022), a few alternative, novel methods have been successfully used recently. Glorius et al. (2019) used the ESR storage ring and silicon detectors to measure the ^{124}Xe(p,γ) reaction. Fallis et al. (2020) used the DRAGON recoil separator to measure the ^{76}Se(α,γ) reaction in inverse kinematics. Finally, Lotay et al. (2021) and Williams et al. (2023) were pioneers in their use of a radioactive beam (^{83}Rb) and the EMMA recoil spectrometer to study the ^{83}Rb$(p,\gamma)^{84}$Sr reaction in inverse kinematics. Efforts for α-scattering on exotic isotopes relevant for the γ-process are also underway (Galaviz 2021). These advancements, along with the already established methods, will enable the low-energy nuclear physics community to measure key reaction cross sections in the near future.

Despite this experimental progress, it remains impossible for the foreseeable future to experimentally access all the reaction rates needed in typical γ-process networks, which include thousands of nuclei and several thousand nuclear reaction rates (Arnould & Goriely 2003). Consequently, reaction rates derived from nuclear theory remain crucial. Furthermore, γ-induced reactions play a key role in the γ-process network, but a measurement of (γ,X) reaction cross sections in the laboratory cannot provide the (γ,X) reaction rate under stellar conditions because thermally excited states in the target nucleus play an important role under stellar conditions, but do not contribute in laboratory experiments (for a more detailed discussion, see Rauscher et al. 2013). Instead, the (γ,X) reaction rates are calculated from the (X,γ) capture rates using the detailed balance relation between forward and backward reaction rates (see e.g. Rauscher & Thielemann 2000). For heavy nuclei, the statistical model is appropriate and widely used to derive reaction rates. In the following paragraphs we briefly discuss this approach, as well as the relevant ingredients and the resulting uncertainties for the reaction rates. We note that, instead, the determination of the astrophysical reaction rates involving low Z p-nuclei may be influenced by effects that cannot be taken into account by the statistical model (Gyürky et al. 2014). Therefore, in these cases, the experimental determination of the cross section is required.

In general, the cross section σ of a (X,γ) capture reaction (with $X = n, p, \gamma$) in the statistical model is defined by the production cross section of the compound nucleus in the entrance channel and the branching ratio in the exit channel. The production cross section scales with the transmission T_X in the entrance channel. The branching b_γ towards the γ-channel is given by

$T_\gamma / \sum_i T_i$, where the transmissions T_i in the nominator have to take into account all open channels. This leads to the simple proportionality:

$$\sigma(X,\gamma) \sim T_X \times \frac{T_\gamma}{\sum_i T_i} = \frac{T_X T_\gamma}{\sum_i T_i}. \quad (2)$$

This equation allows us to understand the relevance of the essential ingredients of the statistical model, which are the γ-strength function (γ SF), the level density (LD), the nucleon optical model potential (NOMP), and the α-nucleus optical model potential (αOMP). We note that the T_i are calculated from global NOMPs and αOMPs for the particle channels and from the γ SF for the γ-channel. Furthermore, the T_i are composed of the sum over all bound states in the respective residual nuclei, which is approximated by the LD above a certain excitation energy; therefore, all T_i depend implicitly on the LD.

For (n,γ) neutron capture reactions, T_n typically far exceeds all T_i for the other channels. Consequently, $\sum_i T_i \approx T_n$, and (n,γ) from Eq. (2) scales mainly with the transmission T_γ, which itself depends on the γ SF and the LD, but is independent of the NOMP and αOMP. Typically, an uncertainty of a factor of two is estimated for the (n,γ) rates, and this uncertainty was used in recent γ-process studies; (see, e.g., Rapp et al. 2006; Rauscher et al. 2016).

For (p,γ) proton-capture reactions on the neutron-deficient nuclei in the γ-process, Eq. (2) leads to the following. Because of the Coulomb barrier, the transmission T_p is sensitively dependent on the energy. At low energies, corresponding to the Gamow window for the reaction rates, T_p is smaller than T_γ, and the neutron channel is closed ($T_\mathrm{n} = 0$). Thus, $\sum_\mathrm{i} T_\mathrm{i} \approx T_\gamma$, and the (p,γ) cross section scales with T_p, which in turn depends mainly on the NOMP and on the LD, but not on the γ SF. As the NOMP is well studied, for (p,γ) rates a similar uncertainty of a factor of two as in the (n,γ) case is often used (e.g., Rapp et al. 2006; Rauscher et al. 2016), although the main origin of the uncertainty is the NOMP for (p,γ) rates and the γ SF and LD for (n,γ) rates.

The situation for (α,γ) reactions is similar to that for the (p,γ) reactions. Again, because of the Coulomb barrier, T_α is much smaller than T_γ at astrophysically relevant energies, and therefore the (α,γ) cross section scales with T_α and becomes mainly sensitive to the αOMP, but is almost completely independent of the γ SF and NOMP. Because of the higher Coulomb barrier, the sensitivity to αOMP is far more pronounced than the sensitivity to NOMP in the (p,γ) case. Much larger uncertainties of a factor of ten or more were found from the comparison between experimental and calculated (α,γ) cross sections; see for example Somorjai et al. (1998). An uncertainty of a factor of ten was used for (α,γ) rates in the above-mentioned γ-process studies (Rapp et al. 2006; Rauscher et al. 2016). It is interesting to note that (α,n) reaction rates also depend essentially only on the αOMP, and a recent study of the weak r-process (Bliss et al. 2020) also used a factor of ten uncertainty for the (α,n) reaction rates. Recently, the origin of this strong sensitivity was better understood (Mohr et al. 2020), and updated reaction rates with an estimated uncertainty of a factor of two using the ATOMKI-V2 αOMP were provided in Mohr et al. (2021). This factor uncertainty was chosen due to the success of ATOMKI-V2 αOMP in reproducing experimentally determined cross sections of α-induced reactions (e.g. Szegedi et al. 2021). Using these updated (α,n) rates, significant progress in the modelling of the weak r-process was achieved (Psaltis et al. 2022).

Summarising the status of theoretical reaction rates from the statistical model, nowadays uncertainties of a factor of two are considered for the rates of the (n,γ), (p,γ), and (α,γ) capture reactions. Because of the relation between forward and reverse reaction rates, this uncertainty of a factor of two also holds for the (γ,n), (γ,p), and (γ,α) photo-disintegration rates. Experimental confirmation of these claimed uncertainties should become possible at least in some well-selected cases with the increasing availability of radioactive ion beams and up-to-date detection techniques. Overall, the new (α,γ) and (γ,α) reaction rates in Mohr et al. (2021) are significantly lower than the widely used rates by Rauscher & Thielemann (2000), in particular for relatively heavy nuclei and lower temperatures. This clearly calls for further investigation, and we will present in future work.

6. Discussion and conclusions

We studied the production of p-nuclei in five different sets of CCSNe. Each set includes the yields from three massive star progenitors with initial masses of 15, 20, and 25 $M_\odot$. We analysed both the overproduction factor of each isotope (relative to their averages, as defined in several different ways) and the ratios of p-nuclei close to each other in mass, relative to their solar ratio. This strategy allowed us to investigate the differences among the different sets of models both in terms of the production site and the nuclear physics.

The different sets of CCSN models present several discrepancies both in the overproduction factors and their ratios. These depend on (i) the assumptions on stellar physics implemented in each set, that is, the adoption of different criteria for convection, mass-loss prescriptions, the use of overshooting, the explosion mechanism, and so on, and (ii) the different nuclear physics inputs. The different assumptions in stellar modelling mostly influence the final pre-supernova structure of the star, as well as the possibility of having merger events in the advanced phases of the pre-supernova evolution. The variations in the stellar structure also lead to different modalities of the propagation of the shock wave during the supernova explosion and hence to different explosive nucleosynthesis. The use of different nuclear physics inputs leads to local variations in the proportions of the isotopes of nearby mass, mostly influencing the isotopic ratios.

In Sect. 3, we discuss the finding that the F_0 is not appropriate as a general tool to investigate the properties of the γ-process nucleosynthesis. Alternative definitions of this parameter can help us to distinguish the production of p-nuclei from different nucleosynthetic processes, but these are still not sufficient to allow us to study the details of the γ-process in the models. For this reason, we analysed the correlations between 12 different couples of OP ratios of isotopes close in mass.

Ten of the considered isotopic ratios show good agreement with the solar ratio for most of the models. These are ^{74}Se/^{78}Kr and ^{84}Sr/^{78}Kr (Appendix B.1), ^{102}Pd/^{108}Cd and ^{106}Cd/^{108}Cd (Appendix B.3), ^{120}Te/^{126}Xe and ^{124}Xe/^{126}Xe (Appendix B.5), ^{130}Ba/^{132}Ba and ^{136}Ce/^{138}Ce (Appendix B.6), ^{144}Sm/^{132}Ba (Appendix B.7), and ^{174}Hf/^{180}W (Appendix B.10). The other 13 ratios show no agreement with solar and/or one or both isotopes have an insufficient overproduction factor for their origin to be attributed to the γ-process in CCSNe. In particular, the p-only Mo and Ru isotopes are not produced in any of the considered models and their origin remains a mystery. Nuclei such as ^{113}In, ^{115}Sn, ^{138}La, ^{152}Gd, and ^{164}Er are not significantly produced by the γ-process, which confirms that the bulk of their abundance in the Solar System is provided by other processes. We also notice that ^{74}Se, ^{78}Kr, and ^{84}Sr can be explained by the γ-process only, without requiring an α-rich freeze-out contribution.

The effect of the C–O shell mergers is mostly to increase the abundances of the p-nuclides heavier than Pd. In the case of the p-nuclei lighter than Pd, that is, those belonging to Se, Kr, Sr, Mo, and Ru, the yield is completely dominated by the explosion and models with C–O mergers do not significantly differ from the standard models. Moreover, these events typically favour the production of the most neutron-rich isotope within p-only pairs belonging to the same element. This is a signature of a γ-process that occurs at lower temperature, as compared to the explosive conditions.

In conclusion, we show that a large scatter among the existing CCSN model production exists and no set of models is able to perfectly reproduce the distribution of the p-nuclei measured in the Solar System. As most of the models adopt outdated nuclear reaction rates, our results highlight the need for an upgrade of the γ-process nucleosynthesis nuclear networks with the latest results in nuclear physics, as discussed in Sect. 5. Furthermore, it is generally assumed that γ-process yields from CCSNe depend only weakly on the energy of the explosion, however there are no detailed studies that confirm this. Therefore, we will proceed to improve and update our γ-process nuclear network to compute new massive stars and CCSN models for a wide grid of explosion energies in order to further investigate the γ-process nucleosynthesis in massive stars.

Acknowledgements. We thank the support from the NKFI via K-project 138031 and the ERC Consolidator Grant (Hungary) programme (RADIOSTAR, G.A. n. 724560). L.R. and M.P. acknowledge the support to NuGrid from JINA-CEE (NSF Grant PHY-1430152) and STFC (through the University of Hull's Consolidated Grant ST/R000840/1), and ongoing access to `viper`, the University of Hull High Performance Computing Facility. L.R. acknowledges the support from the ChETEC-INFRA – Transnational Access Project 22102724-ST. M.P. and M.L. acknowledge the support from the "Lendület-2014" Programme of the Hungarian Academy of Sciences (Hungary). A.P. acknowledges support from US Department of Energy, Office of Science, Office of Nuclear Physics, under Award Number DE-SC0017799 and Contract Nos. DE- FG02-97ER41033 and DE-FG02-97ER41042. A.S. acknowledges funding by the European Union's Framework Programme for Research and Innovation Horizon Europe under Marie Sklodowska-Curie grant agreement No. 101065891. P.M., Gy. Gy., and Zs. F. acknowledge support from National Research Development and Innovation Office (NKFIH), Budapest, Hungary (K134197). This work was supported by the European Union's Horizon 2020 research and innovation programme (ChETEC-INFRA – Project no. 101008324), and the IReNA network supported by US NSF AccelNet (Grant No. OISE-1927130).

References

Anders, E., & Grevesse, N. 1989, Geochim. Cosmochim. Acta, 53, 197
Andrassy, R., Herwig, F., Woodward, P., & Ritter, C. 2019, MNRAS, 2556
Andrews, S., Fryer, C., Even, W., Jones, S., & Pignatari, M. 2020, ApJ, 890, 35
Arcones, A., & Montes, F. 2011, ApJ, 731, 5
Arlandini, C., Käppeler, F., Wisshak, K., et al. 1999, ApJ, 525, 886
Arnould, M. 1976, A&A, 46, 117
Arnould, M., & Goriely, S. 2003, Phys. Rep., 384, 1
Asplund, M., Grevesse, N., Sauval, A. J., & Scott, P. 2009, ARA&A, 47, 481
Bao, Z. Y., Beer, H., Käppeler, F., et al. 2000, At. Data Nucl. Data Tables, 76, 70
Battino, U., Pignatari, M., Travaglio, C., et al. 2020, MNRAS, 497, 4981
Bisterzo, S., Gallino, R., Straniero, O., Cristallo, S., & Käppeler, F. 2011, MNRAS, 418, 284
Bisterzo, S., Travaglio, C., Gallino, R., Wiescher, M., & Käppeler, F. 2014, ApJ, 787, 10
Bisterzo, S., Gallino, R., Käppeler, F., et al. 2015, MNRAS, 449, 506
Bliss, J., Arcones, A., Montes, F., & Pereira, J. 2020, Phys. Rev. C, 101, 055807
Burbidge, E. M., Burbidge, G. R., Fowler, W. A., & Hoyle, F. 1957, Rev. Mod. Phys., 29, 547
Byelikov, A., Adachi, T., Fujita, H., et al. 2007, Phys. Rev. Lett., 98, 082501
Cameron, A. G. W. 1957, AJ, 62, 9
Caughlan, G. R., & Fowler, W. A. 1988, At. Data Nucl. Data Tables, 40, 283
Cheng, H., Sun, B.-H., Zhu, L.-H., et al. 2021, ApJ, 915, 78
Choplin, A., Goriely, S., Hirschi, R., Tominaga, N., & Meynet, G. 2022, A&A, 661, A86
Costa, V., Rayet, M., Zappalà, R. A., & Arnould, M. 2000, A&A, 358, L67
Couch, S. M., & Ott, C. D. 2013, ApJ, 778, L7
Cowan, J. J., Sneden, C., Lawler, J. E., et al. 2021, Rev. Mod. Phys., 93, 15002
Cumming, J. B., & Alburger, D. E. 1985, Phys. Rev. C, 31, 1494
Curtis, S., Ebinger, K., Fröhlich, C., et al. 2018, ApJ, 870, 2
Cyburt, R. 2011, in APS Division of Nuclear Physics Meeting Abstracts, 56, 7
den Hartogh, J., Petö, M. K., Lawson, T., et al. 2022, ApJ, 927, 220
Dillmann, I., Heil, M., & Käppeler, F. 2006, AIP Conf. Ser., 819, 123
Dillmann, I., Käppeler, F., Rauscher, T., et al. 2008, Nuclei in the Cosmos (NIC X), 91
Eggenberger, P., Meynet, G., Maeder, A., et al. 2008, Astrophys. Space Sci., 316, 43
Eichler, M., Nakamura, K., Takiwaki, T., et al. 2017, J. Phys. G Nucl. Part. Phys., 45, 014001
Fallis, J., Akers, C., Laird, A. M., et al. 2020, Phys. Lett. B, 807, 135575
Foteinou, V., Harissopulos, S., Axiotis, M., et al. 2018, Phys. Rev. C, 97, 035806
Fröhlich, C., Hix, W. R., Martínez-Pinedo, G., et al. 2006, New Astron. Rev., 50, 496
Fryer, C., Benz, W., Herant, M., & Colgate, S. A. 1999, ApJ, 516, 892
Fryer, C. L., Belczynski, K., Wiktorowicz, G., et al. 2012, ApJ, 749, 91
Fryer, C. L., Andrews, S., Even, W., Heger, A., & Safi-Harb, S. 2018, ApJ, 856, 63
Fülöp, Z., Kiss, A. Z., Somorjai, E., et al. 1996, Z. Physik A - Hadrons and Nuclei, 335, 203
Galaviz, D. 2021, α-scattering on Unstable Proton-rich tin Isotopes in Inverse Kinematics for the Astrophysical p-process, Tech. rep., CERN, Geneva
Ghosh, S., Wolfe, N., & Fröhlich, C. 2022, ApJ, 929, 43
Glorius, J., Langer, C., Slavkovská, Z., et al. 2019, Phys. Rev. Lett., 122, 092701
Goriely, S., & Siess, L. 2001, A&A, 378, L25
Grevesse, N., & Noels, A. 1993, in Origin and Evolution of the Elements, eds. N. Prantzos, E. Vangioni-Flam, & M. Casse (Cambridge : Cambridge University Press), 15
Gyürky, G., Vakulenko, M., Fülöp, Z., et al. 2014, Nucl. Phys. A, 922, 112
Gyürky, G., Fülöp, Z., Käppeler, F., Kiss, G. G., & Wallner, A. 2019, Eur. Phys. J. A, 55, 41
Harissopulos, S., Vagena, E., Dimitriou, P., et al. 2021, Phys. Rev. C, 104, 025804
Harris, J. A., Hix, W. R., Chertkow, M. A., et al. 2017, ApJ, 843, 2
Heger, A., & Woosley, S. E. 2010, ApJ, 724, 341
Heim, F., Scholz, P., Mayer, J., Müller, M., & Zilges, A. 2020, Phys. Rev. C, 101, 035807
Hillebrandt, W., Kromer, M., Röpke, F. K., & Ruiter, A. J. 2013, Front. Phys., 8, 116
Jones, S., Röpke, F. K., Fryer, C., et al. 2019, A&A, 622, A74
Käppeler, F., Gallino, R., Bisterzo, S., & Aoki, W. 2011, Rev. Mod. Phys., 83, 157
Kelmar, R., Simon, A., Olivas-Gomez, O., et al. 2020, Phys. Rev. C, 101, 015801
Khaliel, A., Mertzimekis, T. J., Asimakopoulou, E. M., et al. 2017, Phys. Rev. C, 96, 035806
Korkulu, Z., Özkan, N., Kiss, G. G., et al. 2018, Phys. Rev. C, 97, 045803
Lawson, T. V., Pignatari, M., Stancliffe, R. J., et al. 2022, MNRAS, 511, 886
Lodders, K. 2003, ApJ, 591, 1220
Lotay, G., Gillespie, S. A., Williams, M., et al. 2021, Phys. Rev. Lett., 127, 112701
Meakin, C. A., & Arnett, D. 2006, ApJ, 637, L53
Mohr, P., Fülöp, Z., Gyürky, G., Kiss, G. G., & Szücs, T. 2020, Phys. Rev. Lett., 124, 252701
Mohr, P., Fülöp, Z., Gyürky, G., et al. 2021, At. Data Nucl. Data Tables, 142, 101453
Müller, B., Viallet, M., Heger, A., & Janka, H.-T. 2016, ApJ, 833, 124
Nemeth, Z., Kaeppeler, F., Theis, C., Belgya, T., & Yates, S. W. 1994, ApJ, 426, 357
Nishimura, N., Rauscher, T., Hirschi, R., et al. 2018, MNRAS, 474, 3133
Palmisano-Kyle, A., Spyrou, A., DeYoung, P. A., et al. 2022, Phys. Rev. C, 105, 065804
Paxton, B., Bildsten, L., Dotter, A., et al. 2011, ApJS, 192, 3
Pignatari, M., & Herwig, F. 2012, Nucl. Phys. News, 22, 18
Pignatari, M., Hirschi, R., Wiescher, M., et al. 2013, ApJ, 762, 31
Pignatari, M., Göbel, K., Reifarth, R., & Travaglio, C. 2016a, Int. J. Modern Phys. E, 25, 1630003
Pignatari, M., Herwig, F., Hirschi, R., et al. 2016b, ApJS, 225, 24
Prantzos, N., Hashimoto, M., Rayet, M., & Arnould, M. 1990, A&A, 238, 455
Psaltis, A., Khaliel, A., Assimakopoulou, E. M., et al. 2019, Phys. Rev. C, 99, 065807
Psaltis, A., Arcones, A., Montes, F., et al. 2022, ApJ, 935, 27
Rapp, W., Görres, J., Wiescher, M., Schatz, H., & Käppeler, F. 2006, ApJ, 653, 474

Rauscher, T., & Thielemann, F.-K. 2000, At. Data Nucl. Data Tables, 75, 1
Rauscher, T., Thielemann, F.-K., & Kratz, K.-L. 1997, Phys. Rev. C, 56, 1613
Rauscher, T., Heger, A., Hoffman, R. D., & Woosley, S. E. 2002, ApJ, 576, 323
Rauscher, T., Dauphas, N., Dillmann, I., et al. 2013, Rep. Prog. Phys., 76, 066201
Rauscher, T., Nishimura, N., Hirschi, R., et al. 2016, MNRAS, 463, 4153
Rayet, M., Arnould, M., Hashimoto, M., Prantzos, N., & Nomoto, K. 1995, A&A, 298, 517
Ritter, C., Andrassy, R., Côté, B., et al. 2018a, MNRAS, 474, L1
Ritter, C., Herwig, F., Jones, S., et al. 2018b, MNRAS, 480, 538
Scholz, P., Wilsenach, H., Becker, H. W., et al. 2020, Phys. Rev. C, 102, 045811
Sieverding, A., Martínez-Pinedo, G., Huther, L., Langanke, K., & Heger, A. 2018, ApJ, 865, 143
Somorjai, E., Fülöp, Z., Kiss, A. Z., et al. 1998, A&A, 333, 1112
Szegedi, T. N., Kiss, G. G., Mohr, P., et al. 2021, Phys. Rev. C, 104, 035804
Theis, C., Käppeler, F., Wisshak, K., & Voss, F. 1998, ApJ, 500, 1039
Tinsley, B. M. 1980, Fund. Cosmic Phys., 5, 287
Travaglio, C., Röpke, F. K., Gallino, R., & Hillebrandt, W. 2011, ApJ, 739, 93
Travaglio, C., Gallino, R., Rauscher, T., et al. 2014, ApJ, 795, 141
Travaglio, C., Rauscher, T., Heger, A., Pignatari, M., & West, C. 2018, ApJ, 854, 18
Weaver, T. A., Zimmerman, G. B., & Woosley, S. E. 1978, ApJ, 225, 1021
Williams, M., Davids, B., Lotay, G., et al. 2023, Phys. Rev. C, 107, 035803
Woods, T. E., & Gilfanov, M. 2013, MNRAS, 432, 1640
Woosley, S. E., & Haxton, W. C. 1988, Nature, 334, 45
Woosley, S. E., & Hoffman, R. D. 1992, ApJ, 395, 202
Woosley, S. E., & Howard, W. M. 1978, ApJS, 36, 285
Woosley, S. E., & Weaver, T. A. 1995, ApJS, 101, 181
Woosley, S. E., Hartmann, D. H., Hoffman, R. D., & Haxton, W. C. 1990, ApJ, 356, 272
Wu, D., Wang, N. Y., Guo, B., et al. 2020, Phys. Lett. B, 805, 135431
Xiong, Z., Martínez-Pinedo, G., Just, O., & Sieverding, A. 2023, Phys. Rev. Lett., submitted [arXiv:2305.11050]

Appendix A: OP factors

Here we present the overproduction (OP) factors and their F_0 of the sets of Rauscher et al. (2002), Pignatari et al. (2016b), Ritter et al. (2018b), Sieverding et al. (2018), and Lawson et al. (2022) used in the analysis presented in this work. Figures A.1, A.2, A.3, A.4, and A.5 show the F_i/F_0 and the isotopic OP factor distributions for the models from each set. As discussed in Section 3, we excluded from our analysis the 25 $M_\odot$ from Ritter et al. (2018b) and the 20 $M_\odot$ from Lawson et al. (2022) —because the majority of the OP factors are lower than 1, which is due to the very large remnant mass obtained after the explosion—, and the 25 $M_\odot$ from Pignatari et al. (2016b), because of the low resolution in the γ-process peak abundances. The respective F_{O16} is also reported as a reference.

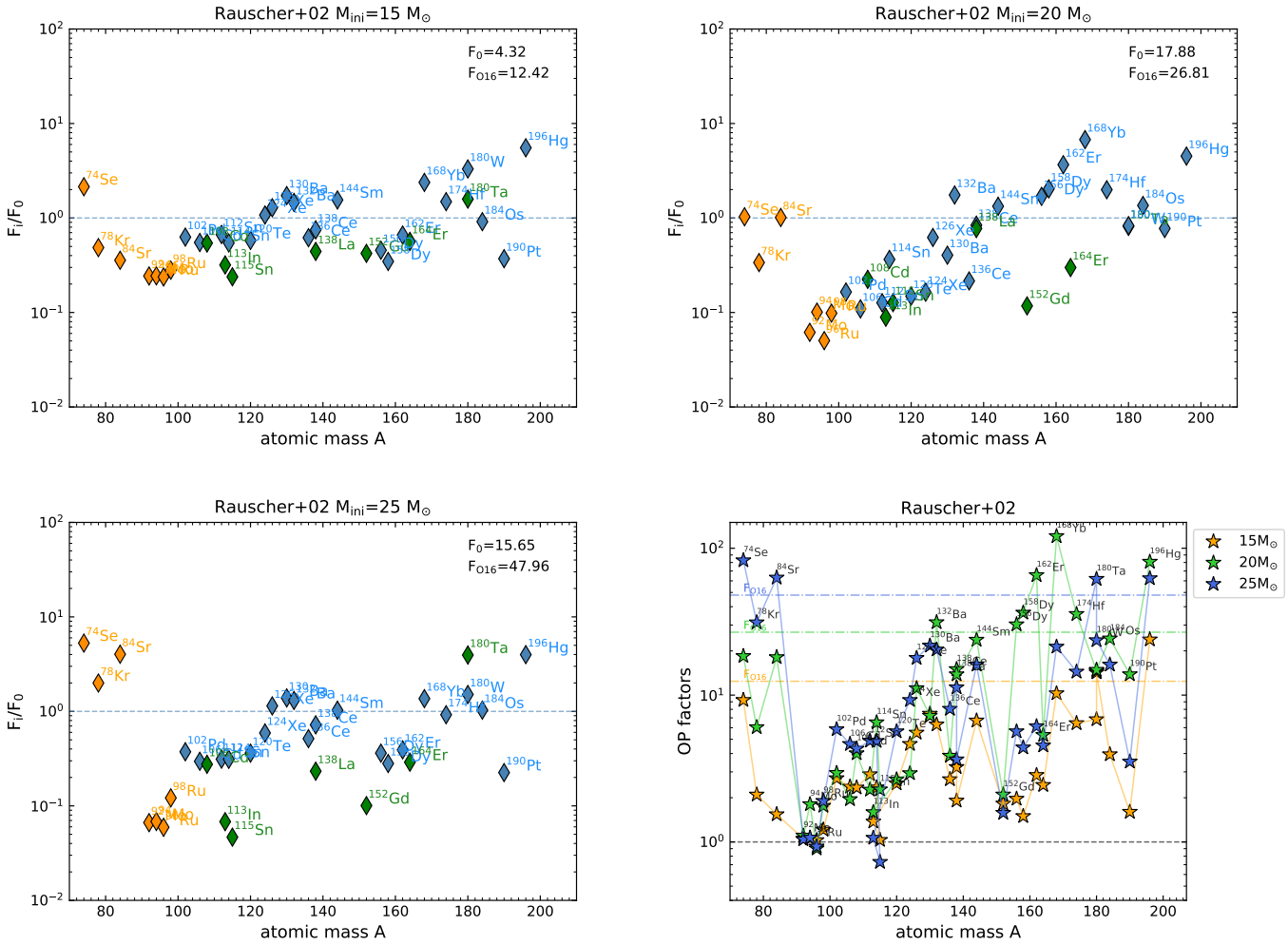

Fig. A.1. The F_i/F_0 of the 15 $M_\odot$ (upper left), 20 $M_\odot$ (upper right), and 25 $M_\odot$ (lower left) progenitors and the isotopic OP factor distributions (lower right) for Rauscher et al. (2002) models. The horizontal dotted-dashed lines in the lower right panel represent the F_{O16} in the 15 (yellow), 20 (green), and 25 $M_\odot$ models (blue).

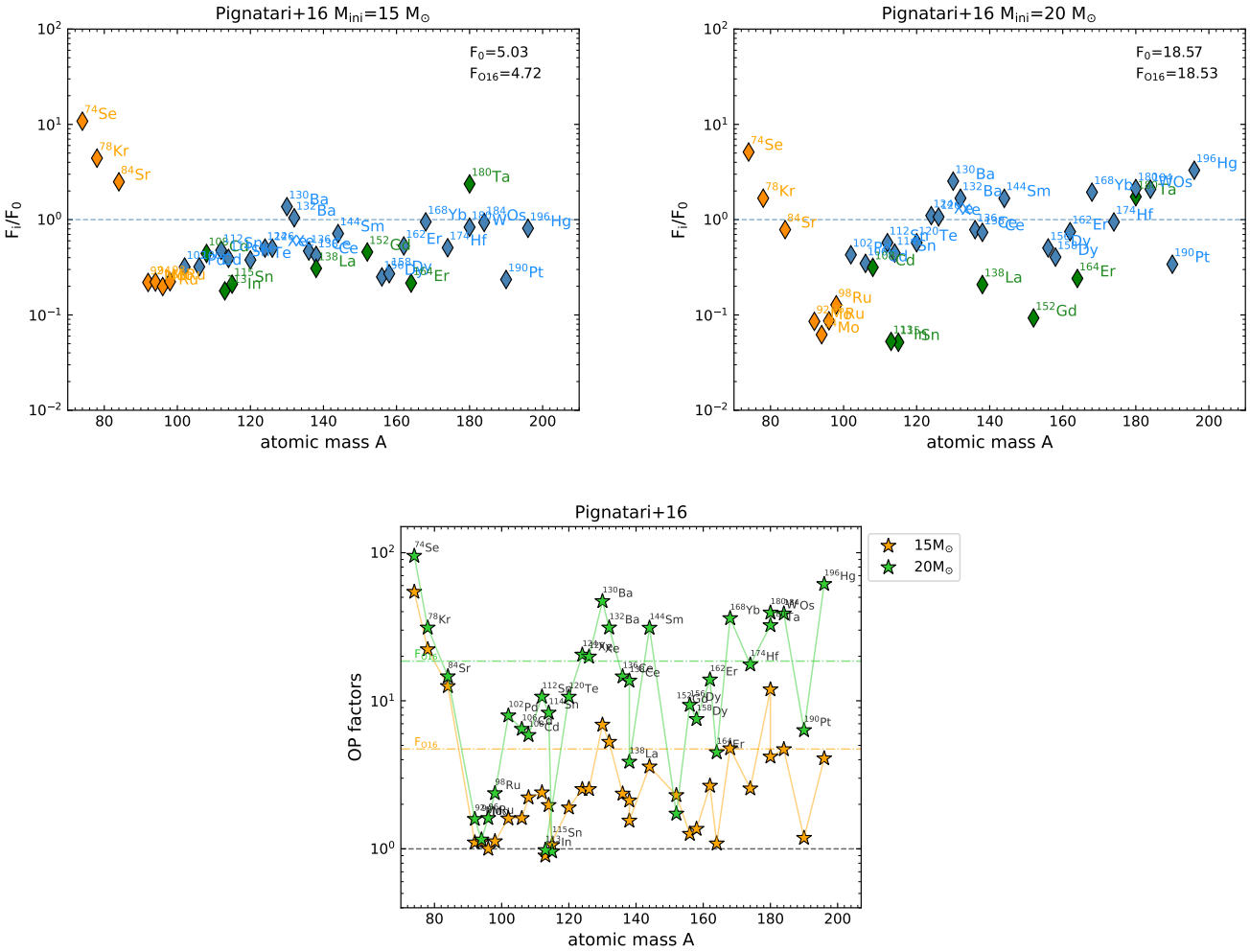

Fig. A.2. Same as Fig. A.1 but for Pignatari et al. (2016b) models.

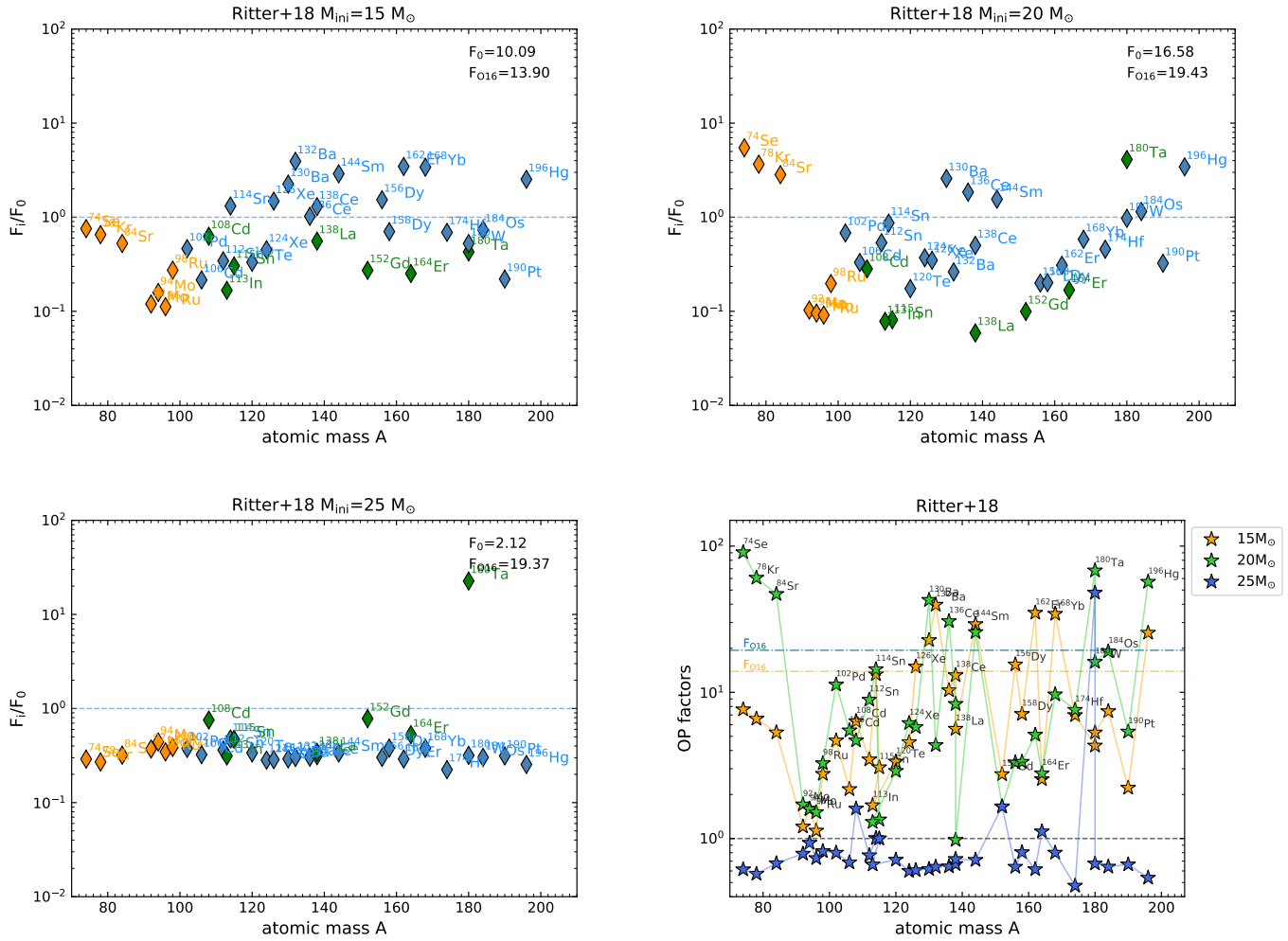

Fig. A.3. Same as Fig. A.1 but for Ritter et al. (2018b) models.

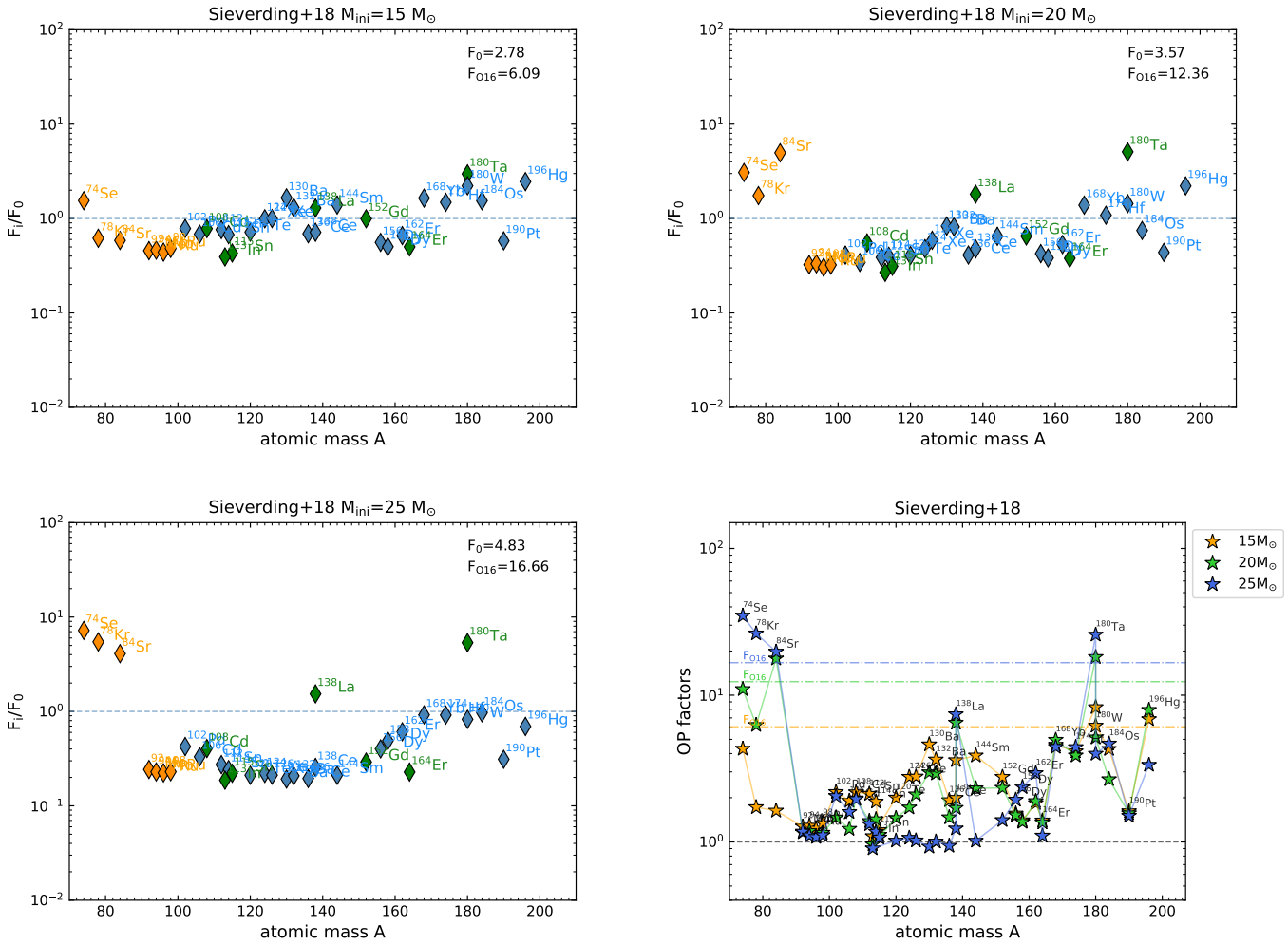

Fig. A.4. Same as Fig. A.1 but for Sieverding et al. (2018) models.

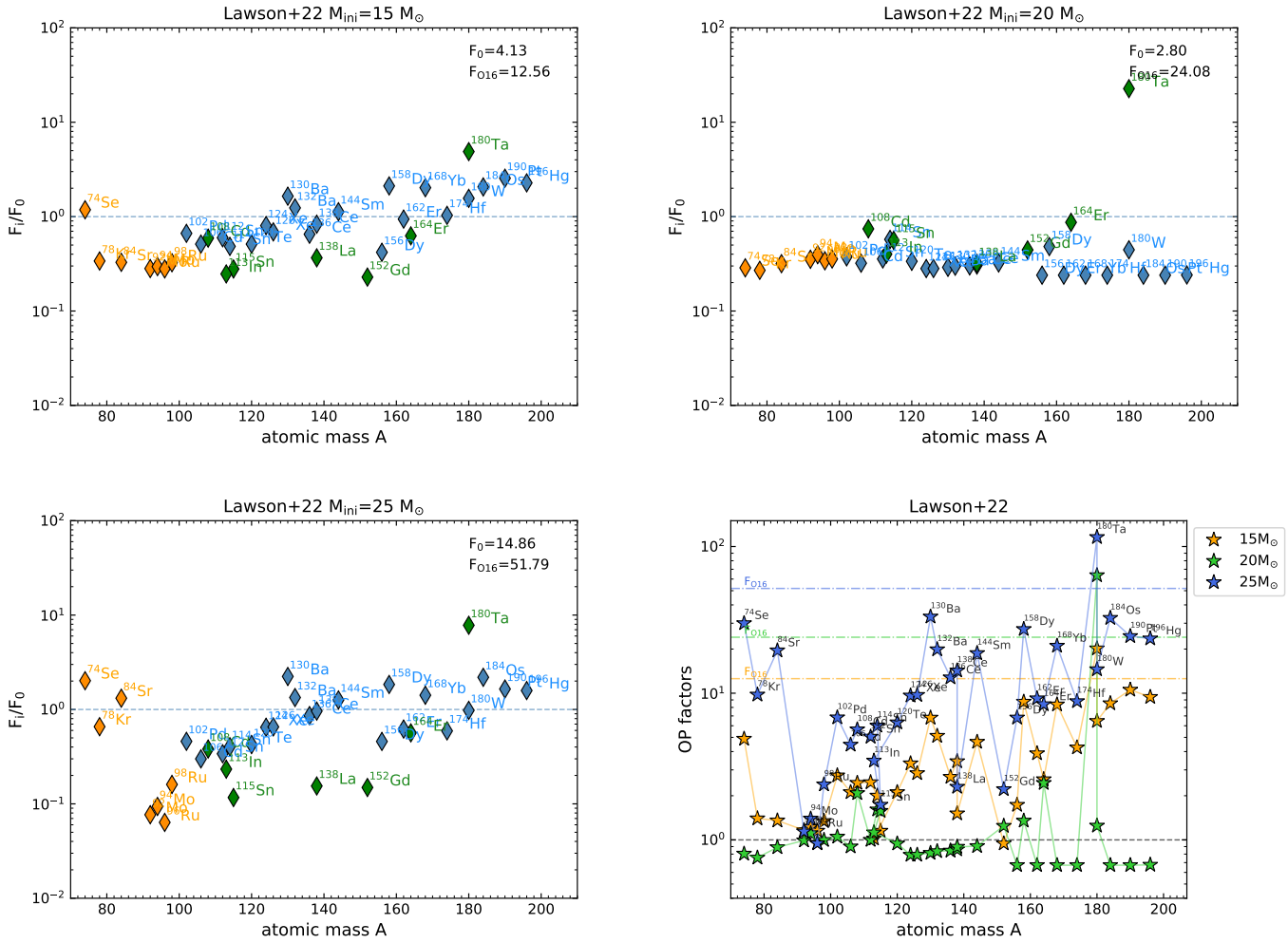

Fig. A.5. Same as Fig. A.1 but for Lawson et al. (2022) models.

Appendix B: Isotopic ratios

Here we present an extended and detailed discussion for 12 couples of isotopic ratios presented in Table 4. The grey regions in the following plots represent regions of values a factor of two and three from the solar ratios. As already stated in Sect. 4, we consider models to be in relatively good agreement with solar when both of the following conditions are satisfied: (i) they fall into the grey areas and (ii) they have an overproduction of at least twice solar (OP > 2).

B.1. ^{74}Se/^{78}Kr *versus* ^{84}Sr/^{78}Kr *(Fig. B.1)*

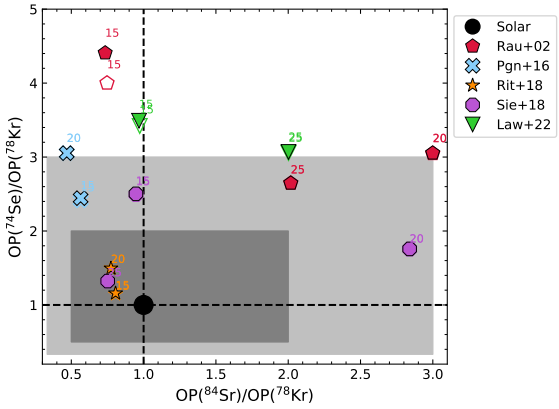

Fig. B.1. isotope[74]Se/^{78}Kr versus ^{84}Sr/^{78}Kr from the model yields, with both ratios normalised to their respective solar values. The light and dark grey shaded areas represent, respectively, values a factor of two and three from the solar ratio (black filled circle). The different sets of models are represented by different types of symbols as indicated in the legend on the right-hand side. The mass of the star is indicated as a small number next to its corresponding symbol. Filled and empty symbols represent the yields including or not, respectively, the radiogenic contribution from all unstable isotopes. The only significant radiogenic contribution comes from ^{74}Br to ^{74}Se.

These two ratios include nuclei that may all have additional channels of production through explosive nucleosynthesis via the α-rich freeze-out and the neutrino-driven winds (see Sects. 1 and 3). In the models considered for this work, the bulk of the yields comes from the γ-process nucleosynthesis occurring in the explosive O/Ne-burning regions. Only the PGN15 model ejects a significant fraction of material from α-rich freeze-out; however, the total yield is still dominated by the O/Ne explosive burning region. Also, in the two models with the C–O shell mergers (RIT15 and RAU20), the explosive γ-process has the most significant contribution to these three isotopes; indeed, the explosion produces about 70%–80% and 40%–60%, respectively, of the total yields (Table 1).

The ^{74}Se/^{78}Kr ratio (y-axis) is always super-solar, that is, OP(^{74}Se) > OP(^{78}Kr). The ^{84}Sr/^{78}Kr ratio (x-axis) of three out of the five 15 $M_\odot$ models (RAU15, SIE15, and LAW15) mostly reflects the initial solar abundances in the envelope of the stars because both OP(^{84}Sr) and OP(^{78}Kr) are lower than 2. In the other two 15 $M_\odot$ models (PGN15 and RIT15), as well as the RIT20 and SIE25 models, instead, ^{78}Kr and ^{84}Sr are significantly produced during the explosive γ-process (see Figures in Appendix A) and therefore the values plotted in the figure represent the γ-process composition, not the initial composition. Among the remaining three 20 $M_\odot$ models, PGN20 produces one of the highest OP(^{78}Kr) of all the models, which leads to the lowest OP(^{84}Sr)/OP(^{78}Kr) ratio. The last two 20 $M_\odot$ models (RAU20 and SIE20) show very similar yields of ^{78}Kr and ^{84}Sr. The solar value of ^{84}Sr/^{78}Kr is instead $\sim$ 0.7, which results in OP(^{84}Sr)/OP(^{78}Kr) being a factor of $\sim$ 3 over the solar ratio. In the 25 $M_\odot$ case, RAU25 and LAW25 show different yields and different OP factors, but the ratio between ^{84}Sr and ^{78}Kr yields is the same, and therefore this leads to a similar behaviour of the ratio of the OP factors.

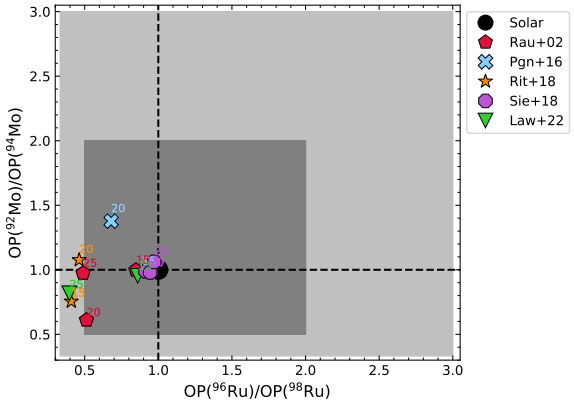

Fig. B.2. Same as Fig. B.1, but for ^{92}Mo/^{94}Mo versus ^{96}Ru/^{98}Ru.

B.2. ^{92}Mo/^{94}Mo *versus* ^{96}Ru/^{98}Ru *(Fig. B.2)*

In almost all models, the OPs of these four isotopes are significantly lower than 2, which confirms that standard massive star models are unable to produce a significant amount of these isotopes. This is why most of the models are in agreement with the solar abundance: they mostly reflect the envelope composition. All the models show a subsolar ^{96}Ru/^{98}Ru ratio (x-axis), while the ^{92}Mo/^{94}Mo ratio (y-axis) is more variable and there are six models where this ratio is roughly a factor of two different from solar. In the case of the two models with C–O shell mergers (RIT15 and RAU20), the production of the more neutron-rich isotopes of each element is favoured, and therefore both plotted ratios are subsolar (Table 1). Out of the other four models different from solar, in RIT20 the γ-process takes place during explosive Ne burning in an extended region of $\sim$ 0.6 $M_\odot$, with a wide γ-process peak, in particular of ^{92}Mo and ^{98}Ru, which results in higher yields of these two isotopes compared to the other models. Instead, in PGN20 there are two distinct γ-process regions, one in the typical O/Ne explosive burning zone and one just above the interface between the ONe and CO cores, where the shock wave accelerates again with a consequent increase in the peak temperature. This double contribution to the γ-process nucleosynthesis increases the OP factors of ^{92}Mo, ^{96}Ru, and ^{98}Ru. However, those features do not significantly affect the overall distribution of the p-nuclei.

B.3. ^{102}Pd/^{108}Cd *versus* ^{106}Cd/^{108}Cd *(Fig. B.3)*

Most of the models fall within a factor of 2 from the solar ratios. The four models RIT15, PGN15, SIE20, and RAU20 all have subsolar ratios and the same ^{102}Pd/^{108}Cd (y-axis). In the case of PGN15 and SIE20, the subsolar ^{102}Pd/^{108}Cd ratio is due to OP(^{102}Pd) < 2, while the other two models (RIT15 and RAU20) are those that experience a C–O shell merger, where the production of ^{108}Cd —which is the denominator in both plotted ratios— is favoured over that of ^{106}Cd and ^{102}Pd. The production

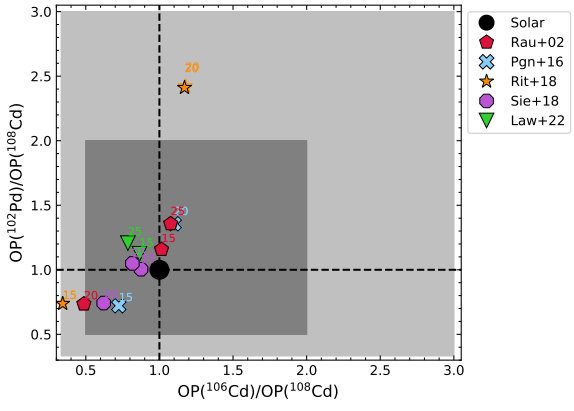

Fig. B.3. Same as Fig. B.1, but for ^{102}Pd/^{108}Cd versus ^{106}Cd/^{108}Cd.

of ^{102}Pd is different between those two C–O shell merger models: in RIT15, it is dominated by the merger and in RAU20 by the explosion (see Table 1). Instead, RAU15/25, PGN20, and RIT20 all have super-solar ratios because their OP(^{102}Pd) and OP(^{106}Cd) (i.e. of the isotopes at the numerator) are significantly higher than the other models, while their OP(^{108}Cd) is similar. All the other models have super-solar ^{102}Pd/^{108}Cd and subsolar ^{106}Cd/^{108}Cd, mostly because OP(^{108}Cd) and OP(^{102}Pd) ∼ 2, while OP(^{106}Cd) < 2. No model falls into the quadrant identified by ^{106}Cd/^{108}Cd > solar and ^{102}Pd/^{108}Cd < solar, which means that ^{102}Pd and ^{106}Cd are always overproduced together.

B.4. ^{112}Sn/^{114}Sn *versus* ^{113}In/^{114}Sn *and* ^{112}Sn/^{114}Sn *versus* ^{115}Sn/^{114}Sn *(Fig. B.4)*

Of the four isotopes discusses here, the production of ^{113}In, ^{114}Sn, and ^{115}Sn can also occur via neutron captures because ^{113}Cd and ^{115}In have an unstable isomer (see Sect. 1 and 3). The galactic chemical evolution (GCE) computation of Bisterzo et al. (2014) found that the *s*-process nucleosynthesis in low-mass AGB stars provides a negligible contribution to these nuclei (0, 0.1, and 4.2%, to ^{113}In, ^{114}Sn, and ^{115}Sn, respectively). The estimated *r*-process contributions to ^{113}In and ^{115}Sn are instead between 2% and 16%, and 60% ± 10%, respectively (see e.g. Dillmann et al. 2008; Nemeth et al. 1994; Theis et al. 1998 and references therein). Therefore, the γ-process nucleosynthesis should have a significant role in the production of all of these isotopes. In Fig. B.4 we account for the neutron-capture contribution to ^{115}Sn only, and subtract its *s*- and *r*-process contributions, because the contributions to the other isotopes are negligible. In general, the values close to the solar ratios do not represent the result of γ-process nucleosynthesis because the yields are dominated by the initial abundances. The cases that do not behave like this are discussed in detail below. Specifically, OP(^{113}In) is lower than 2 in all the models, and therefore ^{113}In/^{114}Sn (x-axis, top panel) is always lower than solar. The models that effectively activate the γ-process are characterised by a radiogenic component to ^{113}In dominated by ^{113}Sn. However, this contribution is never enough to produce OP(^{113}In) > 2.

Figure B.4 shows that the models that have a γ-process component contributing to the isotopes of Sn are typically a factor of two to three above or below the solar value, except for the LAW25 model, which has a significant γ-process component, but the ratios are all close to solar because ^{113}In and ^{114}Sn

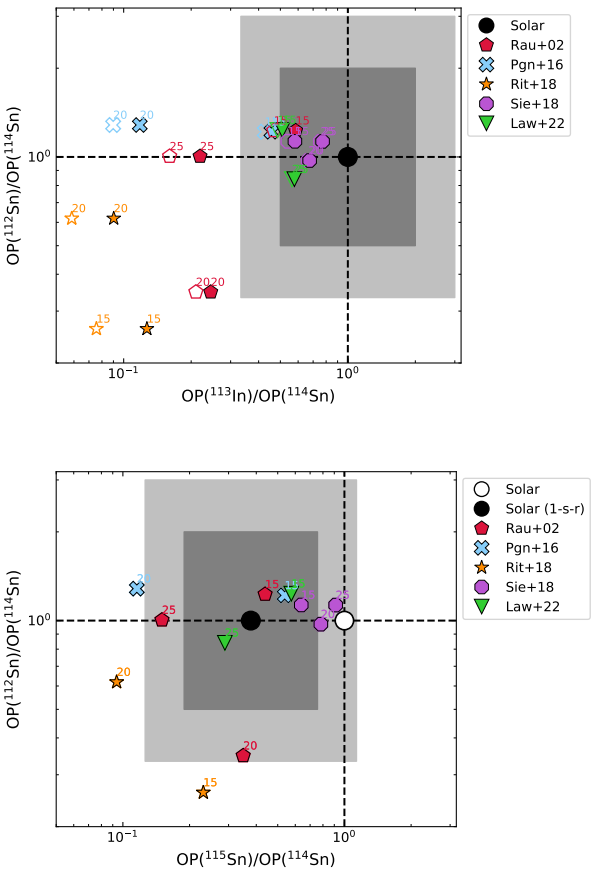

Fig. B.4. Same as Fig. B.1, but for ^{112}Sn/^{114}Sn versus ^{113}In/^{114}Sn (upper panel) and ^{112}Sn/^{114}Sn versus ^{115}Sn/^{114}Sn (lower panel). ^{113}In has a radiogenic contribution from ^{113}Sn. In the lower panel, the empty circle represents the solar ratio, while the filled circle represents the solar ratio minus the *s*- and *r*-process contribution to ^{115}Sn (1-*s*-*r*). In this plot, the grey-shaded areas identify a factor of 2 (dark grey) and 3 (light grey) from the ratio calculated using the (1-*s*-*r*) value.

are similarly overproduced by an *s*-process component in the C shell, and therefore ^{112}Sn/^{114}Sn is slightly subsolar.

Out of the five most extreme models, the C–O shell merger in the RIT15 and RAU20 models favours the production of the more neutron-rich Sn isotopes, which results in subsolar ^{113}In/^{114}Sn and ^{112}Sn/^{114}Sn ratios. The other three most extreme models (PGN20, RIT20 and RAU25) have the highest OP(^{112}Sn) and OP(^{114}Sn) and therefore their ^{113}In/^{114}Sn ratio (top panel, x-axis) is strongly subsolar. In PGN20, the OP(^{112}Sn) dominates over OP(^{114}Sn). This is due to the peculiar structure of this star (see Sec. 2), which has two distinct abundance peaks of γ-process nucleosynthesis, in both of which the abundance of ^{112}Sn is higher than the abundance of ^{114}Sn. In RIT20, an additional production of ^{114}Sn occurs in the C shell, and therefore ^{112}Sn/^{114}Sn decreases to a value below solar. In the RAU25 model, OP(^{112}Sn) and OP(^{114}Sn) are similar, and therefore their ^{112}Sn/^{114}Sn ratio is close to one.

In the lower panel of Fig. B.4, the y-axis is the same as in the top panel, in the x-axis ^{115}Sn substitutes ^{113}In, and the discussion is similar. Moreover, OP(^{115}Sn), as in OP(^{113}In), is always lower than 2, except in the case of the C–O shell merger. Most of the models, including those that have a significant γ-process production, fall within a factor of 3 of the value derived by subtracting the neutron-capture contributions from the solar value.

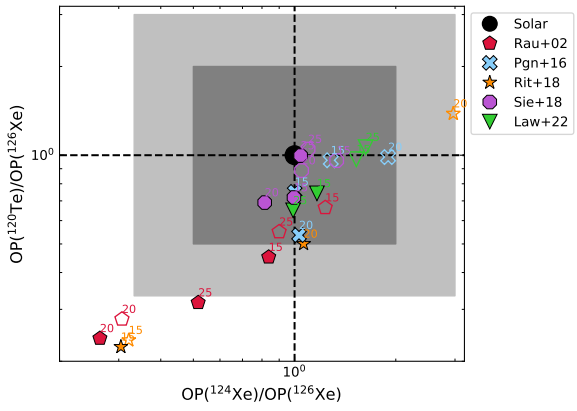

Fig. B.5. Same as Fig. B.1, but for ^{120}Te/^{126}Xe versus ^{124}Xe/^{126}Xe ratio. ^{126}Xe has a radiogenic contribution from ^{126}Ba and ^{126}Cs.

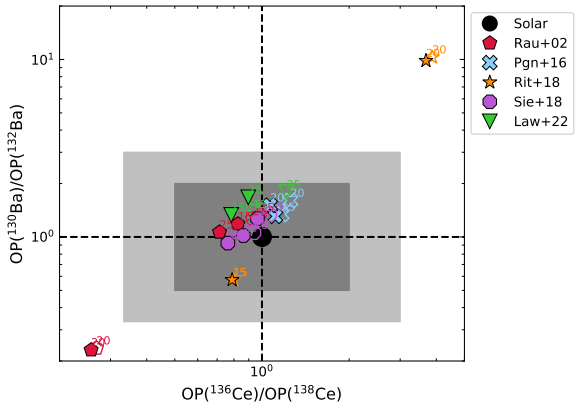

Fig. B.6. Same as Fig. B.1, but for ^{130}Ba/^{132}Ba versus the ^{136}Ce/^{138}Ce ratio. ^{132}Ba and ^{138}Ce have radiogenic contributions from ^{132}Ce, ^{132}La and ^{138}Nd, respectively.

B.5. ^{120}Te/^{126}Xe *versus* ^{124}Xe/^{126}Xe *(Fig. B.5)*

Most of the models move to a subsolar ^{120}Te/^{126}Xe (y-axis) and solar ^{124}Xe/^{126}Xe (x-axis) once the radiogenic contribution to ^{126}Xe is taken into account. We note that the SIE25 model is close to solar because all the OPs are close to one, and therefore it is not relevant for the γ-process analysis (see Fig. 1). Three models are instead different from solar: RIT15, RAU20, and RAU25. Two of these are the models with a C–O shell merger (RIT15 and RAU20), where we find a similar overproduction of ^{120}Te and ^{124}Xe (i.e. the two isotopes at the numerator), and a larger overproduction of ^{126}Xe. This results in both ^{120}Te/^{126}Xe and ^{124}Xe/^{126}Xebeing more than three times lower than solar. Also in the RAU25 model, the overproduction of ^{126}Xe is larger than that of ^{124}Xe and ^{120}Te; however, in this case OP(^{124}Xe) ~ 2OP(^{120}Te).

B.6. ^{130}Ba/^{132}Ba *versus* ^{136}Ce/^{138}Ce *(Fig. B.6)*

The γ-process nucleosynthesis in the majority of the models accurately reproduces the solar ratios on both axes (although note that as in Sect. B.5, the SIE25 model has all the OP factors close to 1), with two exceptions: RIT20 and RAU20. The RIT20 ratios are both super-solar because of a combination of the higher OPs (~30–40) of the more neutron-deficient isotopes (at the numerator) relative to the lower OPs (~4–8) of the more neutron-rich isotopes (at the denominator). The RAU20 ratios

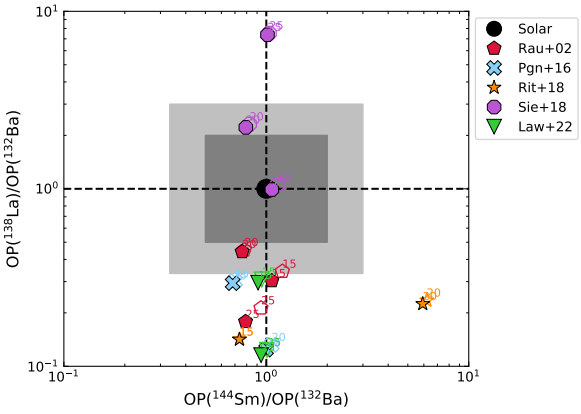

Fig. B.7. Same as Fig. B.1, but for ^{138}La/^{132}Ba versus the ^{144}Sm/^{132}Ba ratio. ^{132}Ba has radiogenic contribution from isotope[132]Ce and ^{132}La.

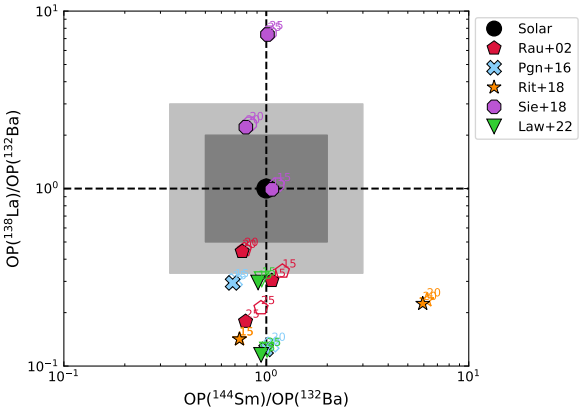

Fig. B.8. Same as Fig. B.1, but for ^{156}Dy/^{152}Gd versus the ^{144}Sm/^{152}Gd ratio. The empty circle represents the solar ratio, while the filled symbol represents the solar ratio minus the *s*-process contribution to the isotope ^{152}Gd (1-*s*). Similarly to Fig. B.4, the grey-shaded areas show a factor 2 and 3 from the ratio calculated using the (1-*s*) value.

are instead both subsolar due to the effect of the C–O shell merger, which favours the more neutron-rich isotopes. The same effect is present in the other model with the C–O shell merger (RIT15), albeit weaker because OP(^{132}Ba) and OP(^{138}Ce) are similar in the two models, while OP(^{130}Ba) and OP(^{136}Ce) are higher in RIT15 than in RAU20.

B.7. ^{138}La/^{132}Ba *versus* ^{144}Sm/^{132}Ba *(Fig. B.7)*

The ^{144}Sm/^{132}Ba ratio (x-axis) in all models falls within a factor of two of the solar value, except for RIT20, where the ^{132}Ba is underproduced. The ^{138}La/^{132}Ba ratio (y-axis) is instead more scattered and in most of the models it is more than three times lower than solar, except for the SIE models. This is because, as mentioned in Sects. 1 and 3, ^{138}La may have an additional neutrino capture contribution, which is only included in the nuclear network of the SIE models. These models also have the lowest OP(^{132}Ba), further contributing to the higher ^{138}La/^{132}Ba ratio.

B.8. ^{156}Dy/^{152}Gd *vs* ^{144}Sm/^{152}Gd *(Fig. B.8)*

Of the three isotopes considered here, as discussed in Sects. 1 and 3, a fraction of the solar abundance of ^{152}Gd comes from the

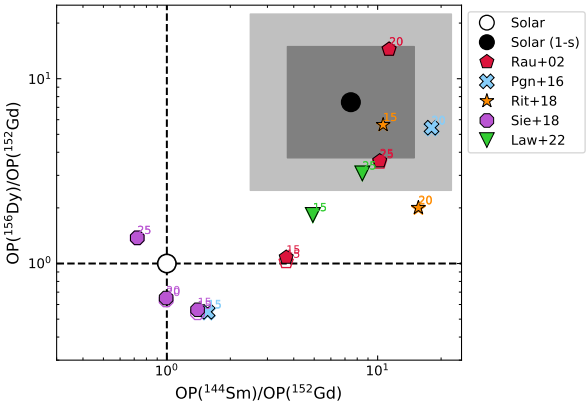

Fig. B.9. Same as Fig. B.1, but for ^{156}Dy/^{158}Dy versus the ^{162}Er/^{164}Er ratio. As in Fig. B.8, the empty circle represents the solar ratio, while the filled symbol represents the solar ratio minus the *s*-process contribution to the isotope ^{164}Er (1-*s*). The grey-shaded areas identify a factor of 2 and 3 from the ratio calculated using the (1-*s*) value.^{158}Dy has a strong radiogenic contribution from ^{158}Er in the LAW models only. ^{164}Er has a radiogenic contribution from ^{164}Yb, and a much less significant contribution from ^{164}Tm. ^{162}Er has a radiogenic contribution from ^{162}Yb.

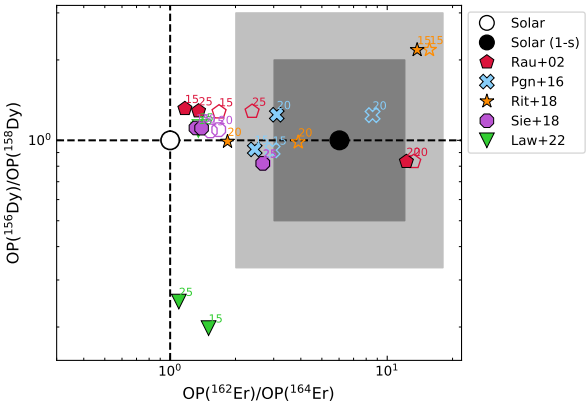

Fig. B.10. Same as Fig. B.1, but for ^{168}Yb/^{180}Ta versus the ^{174}Hf/^{180}W ratio. As in Fig. B.8, the empty circle represents the solar ratio, while the filled symbol represents the solar ratio minus the *s*-process contribution to the isotope ^{180}Ta (1-*s*). The grey-shaded areas identify a factor of 2 and 3 from the ratio calculated using the (1-*s*) value. ^{168}Yb, ^{174}Hf, and ^{180}W have a radiogenic contribution from ^{168}Hf, ^{174}W, and ^{180}Os, respectively. In the RAU models, the same three isotopes have a further radiogenic contribution from ^{168}Lu, ^{174}Ta, and ^{180}Re, respectively.

s-process in AGB stars. The GCE computation of Bisterzo et al. (2014) reported this fraction to be 86.6%. Therefore, in Fig. B.8 we represent the value to be matched as the solar (1-*s*) fraction only, that is, 13.4%. Furthermore, in the models presented here, ^{152}Gd has a dominant *s*-process contribution from the pre-supernova He and C shells and the explosive γ-process component is only a small fraction of the total yield. ^{156}Dy and ^{144}Sm are instead *p*-only nuclei that are produced by γ-process during the explosion, and their OPs are significantly higher than that of ^{152}Gd.

As in the cases of Sects. B.5 and B.6, the SIE25 model is close to solar because all the OPs are close to one, and therefore this is not discussed further. The ^{144}Sm/^{152}Gd ratio (x-axis) of most of the models falls within a factor of three of the ratio calculated with the (1-*s*) value. The three SIE15, SIE20, and PGN15 models, are instead close to the solar ratio because they have OP(^{152}Gd) similar to the other models, but a lower OP(^{144}Sm). The ^{156}Dy/^{152}Gd ratio (y-axis) of five models (RIT15, RAU20/25, PGN20 and LAW25) falls close to the ratio calculated with the (1-*s*) value. Among those, the models with C–O shell mergers (RIT15 and RAU20) show the best agreement. All the other models are closer to solar because they have OP(^{156}Dy) < 2, except for RIT20, where OP(^{156}Dy) ∼ 4.

B.9. ^{156}Dy/^{158}Dy *versus* ^{162}Er/^{164}Er *(Fig. B.9)*

As in the case of ^{152}Gd (Sect. B.8), the solar abundance of ^{164}Er (the denominator of the x-axis) has an *s*-process component (see Sects. 1 and 3). Therefore, here we only focus on the possible γ-process origin of ^{164}Er, which corresponds to 16.6% of its solar abundance (Bisterzo et al. 2014). Five models (PGN15, PGN20, SIE25, plus the two models with C–O shell mergers RIT15 and RAU20) fall within a factor of 3 of the ^{162}Er/^{164}Er ratio calculated with the (1-*s*) value. Unlike in the previous cases (Sec. B.2, B.3, B.4, B.5, and B.6), here the C–O shell merger favours the production of the neutron-deficient ^{162}Er relative to ^{164}Er.

The ^{156}Dy/^{158}Dy ratio (y-axis) is within a factor of 2 from solar, except in the two LAW models, where the radiogenic contribution to ^{158}Dy is higher than in the other models and results in a shift of the ratio to a value more than 4 times lower than solar. We note that, as in the case of the Er isotopes discussed above, the C–O shell merger (in RIT15 and RAU20) favours the production of the neutron-deficient isotope.

B.10. ^{168}Yb/^{180}Ta *versus* ^{174}Hf/^{180}W *(Fig. B.10)*

As in the case of ^{163}Dy (Sec B.9), ^{179}Hf becomes unstable at stellar temperatures, activating a *s*-process branching point. Therefore, ^{180}Ta (and ^{180}W to a lesser extent) may show a neutron-capture contribution due to the chain ^{179}Hf(β^-)^{179}Ta(n,γ)^{180}Ta(β^-)^{180}W. Therefore, we consider only the [(1-*s*) solar] abundance of ^{180}Ta, which is 18.0% (Bisterzo et al. 2014). We note that this residual solar abundance of ^{180}Ta is not only due to the γ-process, because this isotope may also receive a contribution from neutrino-capture on ^{180}Hf (Byelikov et al. 2007; Sieverding et al. 2018). The models mostly populate the region of the plot where the production of ^{180}W and ^{180}Ta dominate, respectively, over the production of ^{174}Hf and ^{168}Yb and they are more than a factor of three below [(1-*s*) solar] ratios. The C–O shell mergers (RIT15 and RAU20), instead, result in the opposite behaviour. Furthermore, these models are within a factor of 3 of the [(1-*s*) solar] ratios.

In all the models models studied here (except the two LAW models), the radiogenic contributions to ^{174}Hf and ^{180}W shift the ^{174}Hf/^{180}W ratio (x-axis) to lower values. In the two LAW models, the ^{180}W yield is instead much larger than the ^{174}Hf yield, which is due to an efficient production of ^{180}W via the *s*-process in the C-shell.

B.11. ^{184}Os/^{196}Hg *versus* ^{190}Pt/^{196}Hg *(Fig. B.11)*

The majority of the models overproduce ^{196}Hg (the denominator in both ratios) relative to ^{184}Os and ^{190}Pt and predict ratios more than three times lower than solar. The main factor responsible for this result is the strong radiogenic contribution from ^{196}Pb to ^{196}Hg. Indeed, without the inclusion of this contribution, most of the models (except the RAU models) fall within a factor of three of the solar ratio. Specifically, these models have OP(^{196}Hg) > OP(^{184}Os) > OP(^{190}Pt). It follows that the discrepancy between

the models and the solar ratios is more severe in the case of ^{190}Pt/^{196}Hg (x-axis), where these models show ratios of between a factor of 4 and 20 lower than solar. For the ^{184}Os/^{196}Hg ratio (y-axis), the most extreme model instead gives a value a factor of 6 lower than solar.

Of the remaining four models closer to the solar ratios (PGN15, SIE25, LAW15, and LAW25), PGN15 and SIE25 have OP(^{190}Pt) < 2 and OP(^{184}Os) > OP(^{196}Hg)> OP(^{190}Pt), while the LAW models behave differently. This is because they have OP(^{190}Pt) significantly higher than the other models, which is also due to the radiogenic contribution of ^{190}Hg and ^{190}Au. Specifically, in LAW15 OP(^{190}Pt) > OP(^{196}Hg) > OP(^{184}Os). In this model, the radiogenic contribution to ^{190}Pt is twice as large as that to ^{196}Hg, and therefore the inclusion of the radiogenic nuclei decreases the ratio by a factor of two. In LAW25, OP(^{184}Os) > OP(^{190}Pt) > OP(^{196}Hg). In this model, the radiogenic contribution to ^{190}Pt and ^{196}Hg is roughly equal, and so the ratio does not change.

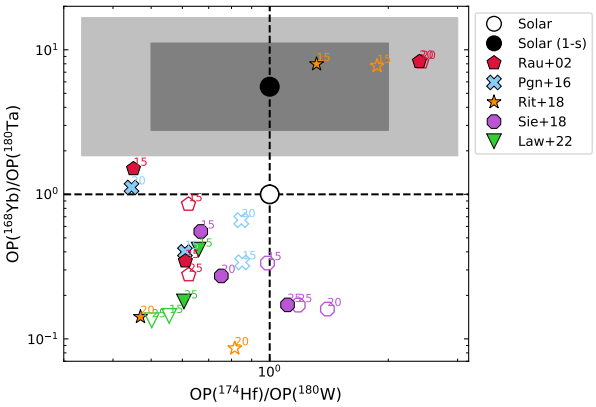

Fig. B.11. Same as Fig. B.1, but for ^{184}Os/^{196}Hg versus the ^{190}Pt/^{196}Hg ratio. ^{196}Hg has a radiogenic contribution from ^{196}Pb and, only in RAU models, from ^{196}Tl. ^{190}Pt has a radiogenic contribution from ^{190}Hg and, only in LAW models, from^{190}Au.